

# CASE 3: SEPARATION CONTROL OVER A WALL-MOUNTED HUMPH

D. Greenblatt, K. B. Paschal, N. W. Schaeffler, A. E. Washburn, J. Harris and C. S. Yao  
*Flow Physics & Control Branch, NASA Langley Research Center, Hampton, VA 23681-2199*

## Introduction

Separation control by means of steady suction [1] or zero efflux oscillatory jets [2] is known to be effective in a wide variety of flows under different flow conditions. Control is effective when applied in a nominally two-dimensional manner, for example, at the leading-edge of a wing or at the shoulder of a deflected flap. Despite intuitive understanding of the flow, at present there is no accepted theoretical model that can adequately explain or describe the observed effects of the leading parameters such as reduced suction-rate, or frequency and momentum input. This difficulty stems partly from the turbulent nature of the flows combined with superimposed coherent structures, which are usually driven by at least one instability mechanism. The ever increasing technological importance of these flows has spurred an urgent need to develop turbulence models with a predictive capability. Present attempts to develop such models are hampered in one way or another by incomplete data sets, uncertain or undocumented inflow and boundary conditions, or inadequate flow-field measurements.

This paper attempts to address these issues by conducting an experimental investigation of a low-speed separated flow over a wall-mounted hump model. The model geometry was designed by Seifert & Pack, who measured static and dynamic pressures on the model for a wide range of Reynolds and Mach numbers and control conditions.[3,4] This paper describes the present experimental setup, as well as the types and range of data acquired. Sample data is presented and future work is discussed.

## Experimental Setup

The experiment consists of wall-mounted Glauert-Goldschmied type body,[3] mounted between two glass endplates where both leading and trailing edges are faired smoothly with a wind tunnel splitter-plate (see fig. 1). This is a nominally two-dimensional experiment, although there are side-wall effects (3-D flow) near the end-plates. The tunnel dimensions at the test section are 771mm wide by 508mm high, but the hump model is mounted on a splitter-plate (12.7mm thick), yielding a nominal test section height of 382mm (distance from the splitter-plate to the top wall). The splitter-plate extends 1935mm upstream of the model's leading-edge. The trailing edge of the splitter-plate, which is 1129mm downstream of the model's leading-edge, is equipped with a flap (95mm long), which is deflected  $24^\circ$  upwards to reduce circulation around the splitter-plate and avoid separation at the leading-edge. The boundary layer is tripped at splitter-plate leading-edge, resulting in a fully-developed turbulent boundary layer ( $\delta \sim 30.5\text{mm}$ ) at 2.14 chord lengths upstream of the model leading-edge. The tunnel medium is air at sea level.

The characteristic reference "chord" length of the model is defined here as the length of the hump on the wall, i.e.  $c=420\text{mm}$ . Seifert & Pack [3] used the body virtual leading-edge to define their chord length; presently the entire hump length is used as the chord length. As a result of this, the current scaled (non-dimensional) coordinates of the overall body shape are slightly different from those of [3]. A simple rescaling operation can recover it.

The model is 584mm wide with endplates at both sides (each approximately 235mm high and 864mm long). The model is 53.7mm high at its maximum thickness point. Both uncontrolled (baseline) and controlled flow scenarios have been considered under various different conditions for  $Re \Omega 1,114,800$  and  $M \Omega 0.12$ . However, detailed flow field measurements were made at  $Re=929,000$ ,  $M=0.100$ . The boundary layer is subjected to a favorable pressure gradient over the front convex portion of the model (fore-body) and separates over a relatively short concave ramp

in the aft part of the body. A slot at approximately the 65% chord station on the model, immediately upstream of the ramp, extends across the entire span ( $s$ ) of the hump. The model was equipped with 165 streamwise and spanwise static pressure ports and 20 dynamic pressure ports in the vicinity of the separated flow region. All pressure transducers were calibrated in-situ prior to each run.

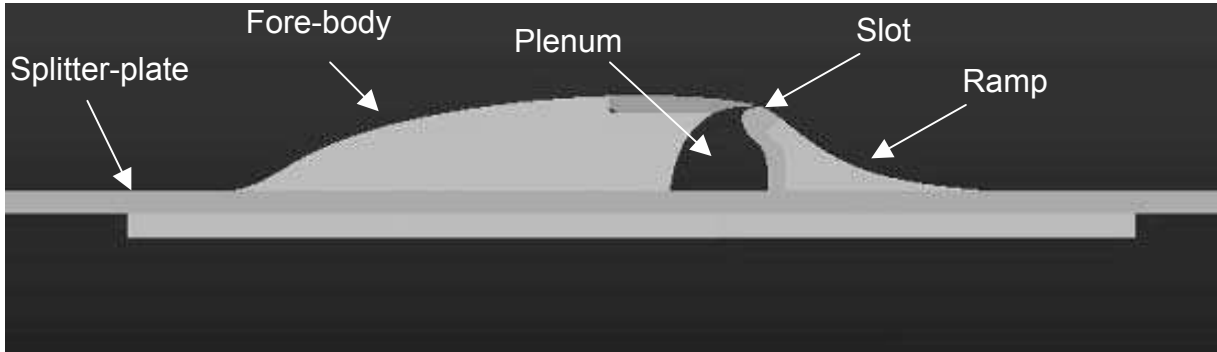


Figure 1: Side view of the model and splitter-plate (endplates not shown)

Separation control is achieved using two methods, namely steady suction and zero efflux oscillatory blowing. Both suction and oscillatory blowing are introduced from the spanwise slot. Steady suction is achieved by means of a suction pump attached to the plenum with the mass flow rate monitored, while zero mass-flux oscillatory suction/blowing is achieved by means of a zero efflux actuator specifically designed to minimize three-dimensional effects near the slot.

## Sample Experimental Data

The primary data acquired for this test case were surface static and dynamic pressures, and two-dimensional and stereo (three-dimensional) PIV in the separated and reattachment regions. Limited hot-wire and Pitot-tube data was acquired as an independent check of the PIV flow field results. An oil-film technique was used to determine the reattachment location. In addition, the inflow boundary layer and upper wall (ceiling) boundary layers were documented.

### Baseline Results

Fig. 2 shows the baseline (no control) surface pressure data, from both dynamic and static pressure ports, in the separated flow region. The figure shows that there is no significant Reynolds number effect for  $Re \geq 557,400$  on this model. Also the extent of the separated region is similar to that of ref. [3] at much higher  $Re$  and a different setup and facility (The reference pressure in [3] was adjusted by 0.266% in order to match their inflow  $C_p$  with the present data). The suction peak upstream of the slot, just downstream of  $x/c=0.5$ , is somewhat higher than that in ref. [3]. The most probable explanation for this is the difference in the ratio of model height to tunnel height for the two cases, namely  $h/H=8\%$  [3] versus 13% (present setup). Fluctuation pressures showed similar trends for all cases. The flow was shown to be essentially two-dimensional in that spanwise pressures did not differ materially in the separated region and planes of stereo PIV flow fields in the separated and reattachment regions showed negligible spanwise variation (see e.g. fig. 3a and 3b). Oil-film surface shear measurements in the reattachment region showed an effectively two-dimensional reattachment line at  $x/c=1.11$  (shown on fig. 2). The static and dynamic pressures are virtually insensitive to the presence of the slot. This was ascertained by comparing data acquired for the open slot (sealed internally at the bottom of the plenum) and the slot sealed externally (not shown).

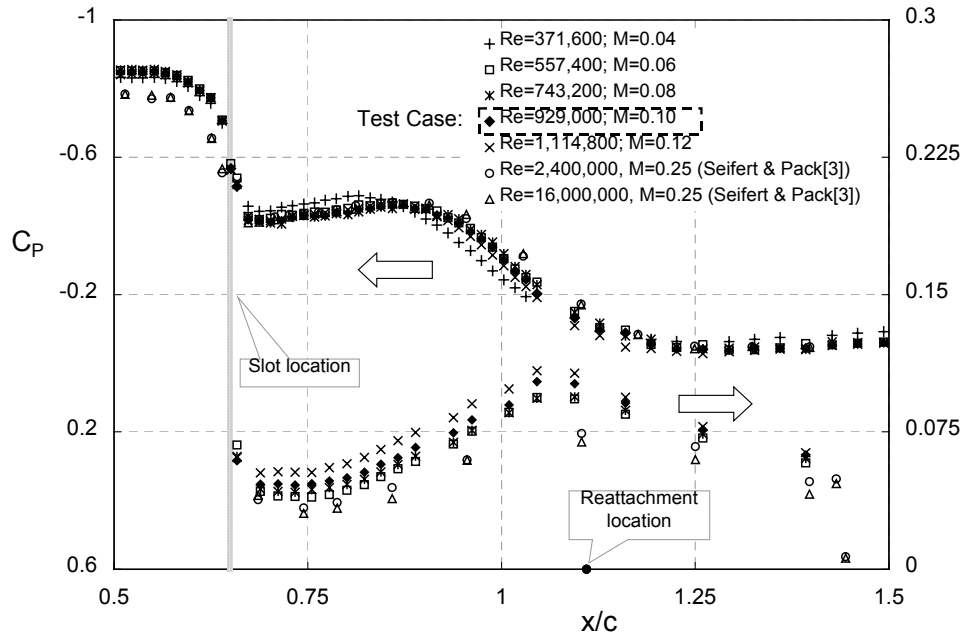


Figure 2. Time-mean and rms surface pressures for the baseline case at various Reynolds numbers.

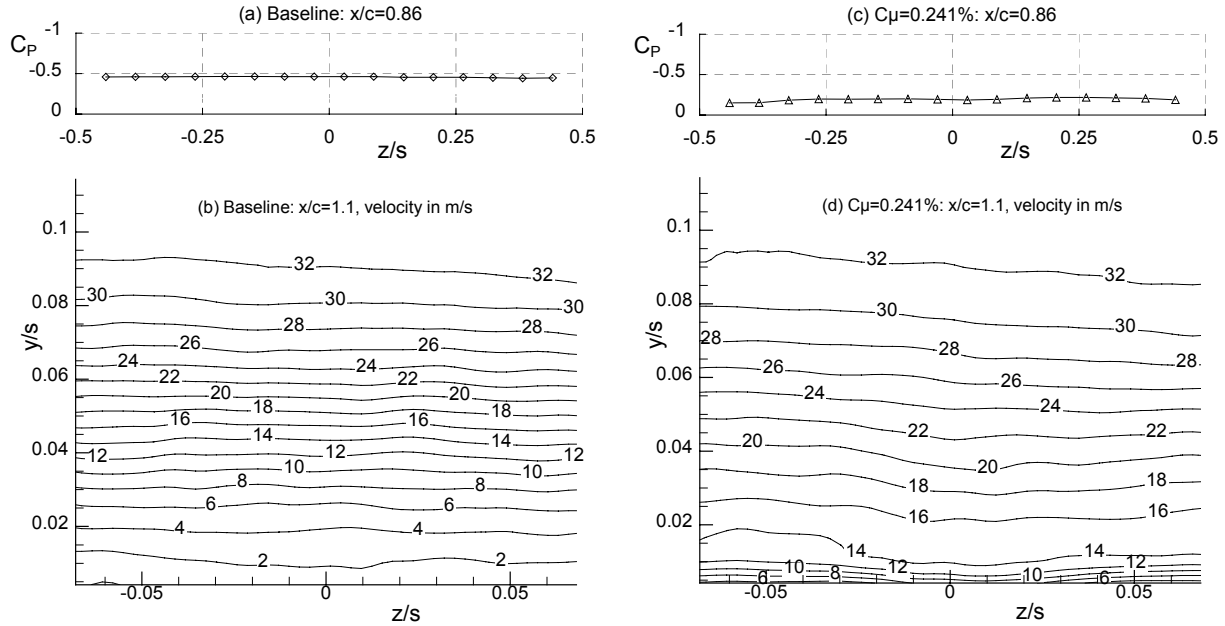


Figure 3. Spanwise ramp pressures and streamwise velocity from stereo PIV in the vicinity of reattachment for the baseline (a,b) and control (c,d) cases.

### Control via Steady Suction

For the suction test case, control was applied via the two dimensional slot using a suction rate of 0.01518 kg/s at  $Re=929,000$ . Furthermore, control was applied for the same dimensionless conditions at different Reynolds numbers (fig. 4). (Suction rates are often expressed as a mass flux coefficient, presently  $C_m=0.15\%$ . Seifert & Pack [3] used  $C_\mu$ , to allow direct comparison with oscillatory cases.) There is a small Reynolds number effect that can be discerned in fig. 3, but the trend is towards the higher Reynolds number data.[3] Additional data acquired at higher suction rates ( $C_\mu \sim 0.456\%$ ) showed similar trends to those at lower  $C_\mu \sim 0.241\%$ . Near the centerline the flow retains its two-dimensional nature (figs. 3c and 3d).

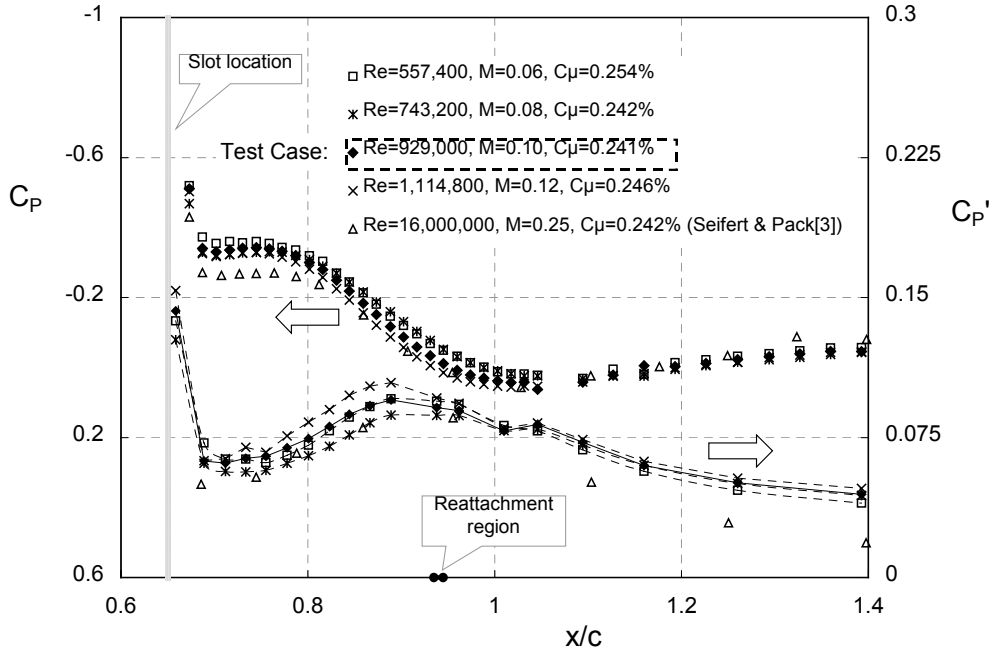


Figure 4. Mean and rms surface pressures for the control case at various Reynolds numbers.

#### PIV Profiles for Baseline & Control Cases

Examples of two-dimensional (2-D) and stereo (three-dimensional) PIV mean velocity profiles, in the vicinity of reattachment, are shown for baseline and steady suction cases in fig. 5.  $U$  is the streamwise component and  $V$  is the component normal to the splitter-plate. Additional 2-D PIV data was acquired from upstream of the slot, continuously throughout the reattachment region. Based on comparisons with Pitot-tube data, errors associated with 2-D profiles were  $\Omega 1\%$  of the maximum velocity, while stereo PIV under-predicted mean velocity profiles by as much as 3% of the maximum.

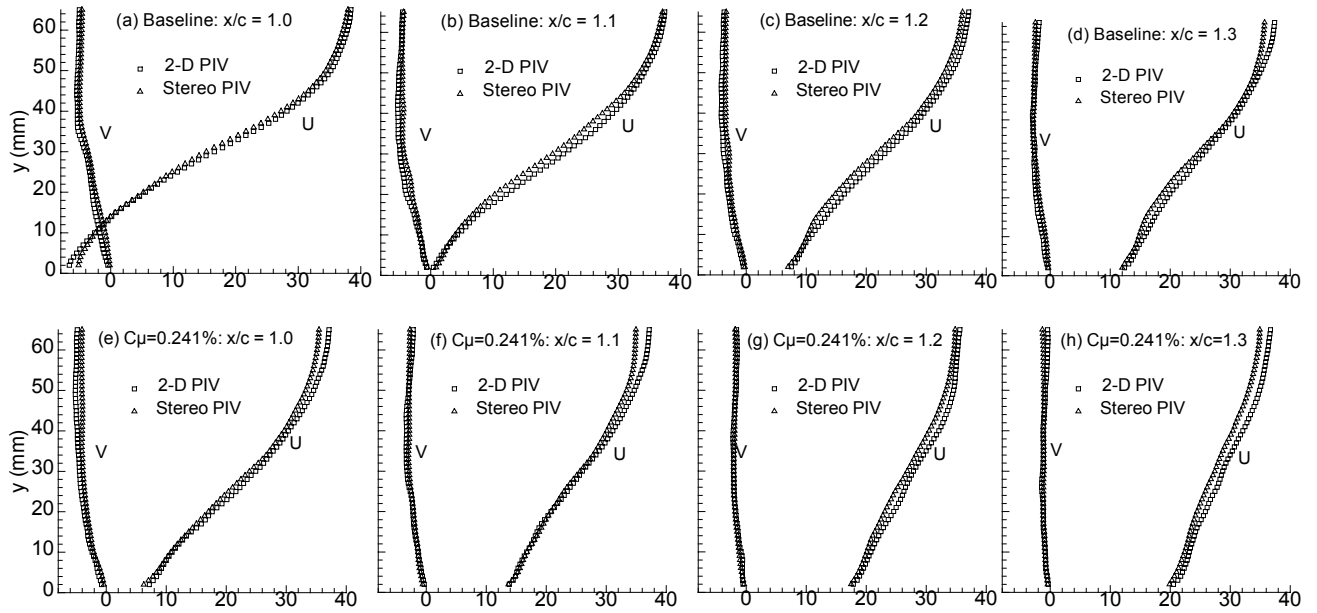


Figure 5. 2-D and Stereo PIV mean velocity profiles for the baseline (a-d) and control (e-h) cases in the vicinity of separation and downstream thereof.

Examples of turbulent stresses, corresponding to the velocity profiles above, are shown in fig. 6. A preliminary error analysis, based on comparisons with hot-wire anemometry indicates errors  $\Omega 20\%$  of the maximum value.

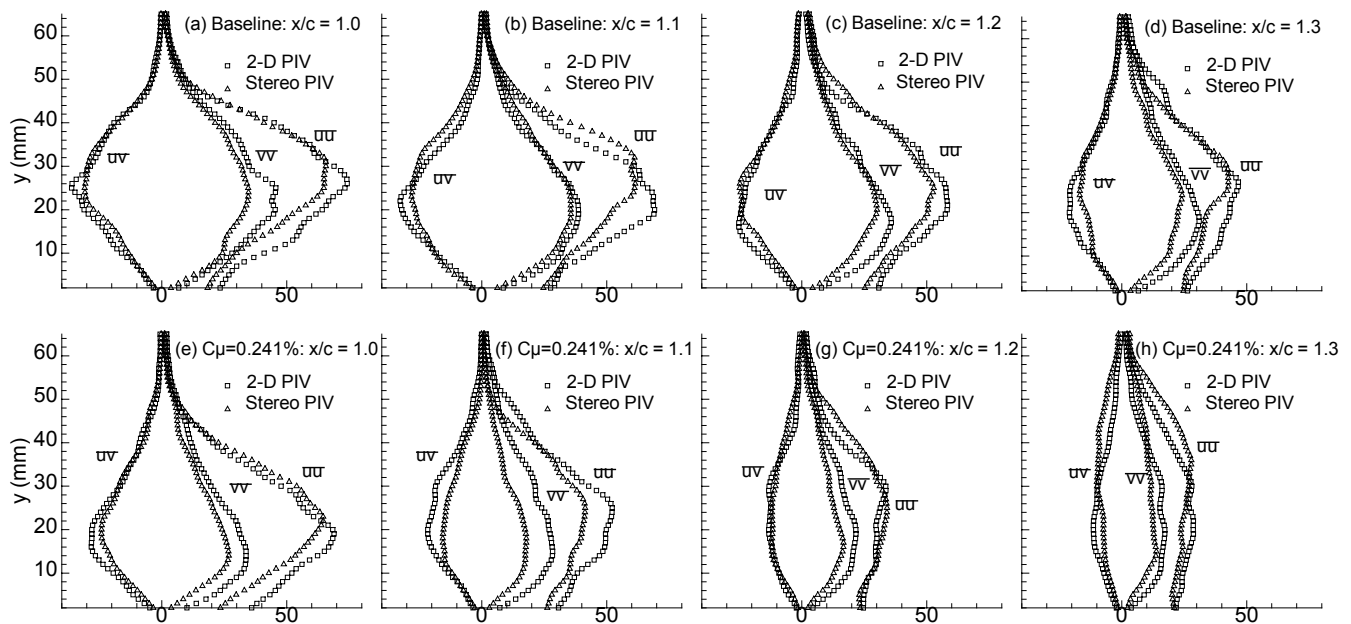


Figure 6. 2-D and Stereo PIV turbulence profiles for the baseline (a-d) and control (e-h) cases in the vicinity of separation and downstream thereof.

## Zero-Efflux Oscillatory Forcing

A zero-efflux oscillatory jet is produced by a rigid piston, that is secured to the base of the plenum by means of a flexible membrane. The piston is driven externally by six voice-coil based actuator modules, providing maximum slot velocities of approximately 80m/s at frequencies ranging from 60Hz to 500Hz. At the test condition (nominal peak slot velocity = 26.6m/s; forcing frequency = 138.5Hz), peak slot velocity measurements vary by less than 3% across the span of the slot. Surface pressures and time resolved flow fields are currently being acquired.

## References

- [1] Lachmann, G. V., "Boundary layer and Flow Control. Its Principles and Application", Volume 1, Pergamon Press, New York, 1961.
- [2] Greenblatt, D. and Wygnanski, I., "Control of separation by periodic excitation", *Progress in Aerospace Sciences*, Volume 37, Issue 7, pp. 487-545, 2000.
- [3] Seifert, A. and Pack, L. G., "Active Flow Separation Control on Wall-Mounted Hump at High Reynolds Numbers," *AIAA Journal*, Vol. 40, No. 7, July 2002.
- [4] Seifert, A. and Pack, L.G., "Effects of Compressibility and Excitation Slot Location on Active Separation Control at High Reynolds Numbers", *Journal of Aircraft* Vol. 40, No. 1, pp. 110-119, Jan-Feb 2003.



## CASE 3: DETAILS AND SUBMISSION GUIDELINES

### Relevant Details

The freestream Mach number is  $M_{\text{freestream}} = 0.10$ . The atmospheric conditions varied, but were essentially standard atmospheric conditions at sea level, in a wind tunnel vented to the atmosphere, in a temperature-controlled room. These conditions can be given as approximately:  $p_{\text{ambient}} = \text{approx } 101325 \text{ kg/(m}\cdot\text{s}^2)$   $T_{\text{ambient}} = \text{approx } 298 \text{ K}$ . Some derived relevant conditions are:  $\text{density}_{\text{ambient}} = \text{approx } 1.185 \text{ kg/m}^3$   $\text{viscosity}_{\text{ambient}} = \text{approx } 18.4\text{e-}6 \text{ kg/(m}\cdot\text{s)}$ ,  $u_{\text{freestream}} = \text{approx } 34.6 \text{ m/s}$ , and  $\text{Re}_{\text{freestream}} = \text{approx } 2.23\text{e}6 \text{ per meter}$ , or  $\text{approx } 9.36\text{e}5 \text{ per chord length of hump}$

The upstream boundary conditions from the experiment (associated with the boundary layer on the plate at location  $x/c = -2.14$  upstream of the start of the hump, where  $c = 16.536 \text{ inches} = 0.4200 \text{ m}$ ), to be used to help set/verify CFD inflow BCs, are given in the following files:

- $u$ -velocity BCs from experiment (pitot probe)
- $\bar{u}'$  streamwise turbulent intensity BCs from experiment (hot wire)
- To complete the Reynolds stress matrix for the upstream BCs at  $x/c = -2.14$ , assume incompressible fully-developed boundary layer distributions

There are two required conditions for case 3: (1) no suction case and (2) suction case. A third oscillatory control case is also defined; however, there is no experimental data available for it yet, so the condition is optional.

- Condition 1: no flow control (no flow through the 23-inch-span slot; slot left *open* with no suction or blowing through it)
- Condition 2: suction rate of  $0.01518 \text{ kg/s}$  ( $27.13 \text{ CFM}$ ) through the 23-inch-span slot (updated 5 September 2003)
- Condition 3 (optional): zero-net-mass-flux oscillatory suction/blowing, frequency =  $138.5 \text{ Hz}$ , peak velocity out of slot ( $U_{\text{jetmax}}$ ) during blowing part of cycle =  $26.6 \text{ m/s}$  (This condition corresponds to an oscillatory blowing momentum coefficient of approximately  $\langle \text{cmu} \rangle = \langle J \rangle / (cq) = \rho \cdot h \cdot (U_{\text{jetrms}})^2 / (c \cdot 0.5 \cdot \rho_{\text{inf}} \cdot U_{\text{inf}}^2) = 0.111\%$ , where  $h$  is the slot width)

### Submission Guidelines

Submissions for this case should include *both* conditions of no-flow-control and steady-suction. The third condition of oscillatory blowing control is optional. The purpose here is to determine the state-of-the-art in modeling these types of flows, so we want to explore which CFD methods work and which do not.

- Either model the internal cavity or specify a boundary condition at the slot exit.
- Either choose to model the flowfield two-dimensionally or three-dimensionally (if three-dimensionally, you may choose to model the endplates or you may employ periodic or some other appropriate spanwise boundary condition).

There is the requirement that the details be specific on how the case is modeled, including all boundary conditions and approximations made. As the methodologies are assessed at the workshop, it will be important to know as many details as possible about the calculations/simulations.

Detailed requirements include:

1. The no-flow-control and steady-suction conditions may be run either time-accurately or in steady-state mode, depending on your computational method. The optional oscillatory blowing control condition (if computed) must be run time-accurately, in order to simulate the unsteady nature of the case.
  - 1a. RANS codes run in time-accurate mode (e.g., URANS) solve directly for phase-averaged variables, i.e.  $\langle u_i \rangle$  and  $\langle u'_i u'_j \rangle$ . Click on [link to PDF write-up](#) or [link to webpage write-up](#) for

more details. Therefore, time-accurate RANS simulations should result in repeating or very-nearly-repeating periodic solutions. When periodicity is achieved, averages over one or more periods of oscillation yields the long-time-averaged (time-independent mean) values for these quantities.

1b. DNS, LES, or DES simulations will need to be post-processed to obtain the long-time-averaged (time-independent mean) values.

2. GRID STUDY: If the case is modeled two-dimensionally, then it is *strongly suggested* that the computation be performed using at least two different grid sizes in order to assess the effect of spatial discretization error on the solution. If it is modeled three-dimensionally, then solutions using more than one grid size are encouraged, but not required. If you use more than one grid, submit each set of results separately.

3. TIME STEP STUDY (for time-accurate computations only): If the case is modeled two-dimensionally, then it is *strongly suggested* that the computation be performed using at least two different time step sizes in order to assess the effect of temporal discretization error on the solution. If it is modeled three-dimensionally, then solutions using more than one time step are encouraged, but not required. If more than one time step is used, submit each set of results separately.

Specific quantities that result from the computations at particular locations will be required for submission. Note that for all the following, the coordinate system with x downstream and y up, with the (x,y)=(0,0) origin at the start of the hump is adopted. All results from 3-D computations are to be given at the z=0 location (centerplane of the tunnel). The chord "c" is the length of the bump: 16.536 inches. For the optional condition 3 (oscillatory control), there is only one submission requirement: the long-time-averaged  $C_p$  (see (e) below). The requirements follow (if is not possible to provide a particular quantity, simply leave it out of the "variable" list, and reduce the number of columns of data submitted):

a.  $x/c$  vs.  $C_p$  on the lower wall for no-flow and suction cases. For time-accurate computations, this should be the long-time-averaged  $C_p$ . The definition for  $C_p$  is  $C_p = (p - p_{inf}) / (0.5 \cdot \rho \cdot u_{inf}^2)$ , where the "inf" values should correspond to the upstream "freestream" location where  $M=0.1$ . Submit these results for both conditions of no-flow-through-the-slot, and for that of constant suction. Include results at least as far upstream as  $x/c = -2.14$ , and at least as far downstream as  $x/c = 2.0$ . Do not include the data on the walls deep inside the slot.

Name this file: case3.cp.ANYTHING.dat-where "ANYTHING" can be any descriptor you choose (should be different for each file if you are submitting multiple runs)-the file should be in 2-column format:

1st line: #your name (pound sign needed)

2nd line: #your affiliation (pound sign needed)

3rd line: #your contact info (pound sign needed)

4th line: #brief description of grid (pound sign needed)

5th line: #brief description of code/method (pound sign needed)

6th line: #other info about the case, such as spatial accuracy (pound sign needed)

7th line: #other info about the case, such as turb model (pound sign needed)

8th line: #other info about the case (pound sign needed)

9th line: variables="x/c"," $C_p$ "

10th line: zone t="surface  $C_p$ , no flow case"

subsequent lines: x/c  $C_p$  <- this is the data for no flow case

next line: zone t="surface  $C_p$ , suction case"

subsequent lines: x/c  $C_p$  <- this is the data for suction case

The sample datafile case3.cp.SAMPLE.dat can be downloaded from the website

b.  $x/c$  vs.  $C_f$  on the lower wall for no-flow and suction cases. For time-accurate computations, this should be the long-time-averaged  $C_f$ . The definition for  $C_f$  is  $C_f = \tau_{aw} / (0.5 \cdot \rho \cdot u_{inf}^2)$ , where the "inf" values should correspond to the upstream "freestream" location where  $M=0.1$ .



The term  $\tau_w$  stands for  $\mu^*(du/dy)$  at the wall. Give these results for both conditions of no-flow-through-the-slot, and that of constant suction. Include results at least as far upstream as  $x/c=-2.14$ , and at least as far downstream as  $x/c=2.0$ . Do not include the data on the walls deep inside the slot. Name this file: case3.cf.ANYTHING.dat -where "ANYTHING" can be any descriptor you choose (should be different for each file if you are submitting multiple runs-the file should be in 2-column format:

1st line: #your name (pound sign needed)  
 2nd line: #your affiliation (pound sign needed)  
 3rd line: #your contact info (pound sign needed)  
 4th line: #brief description of grid (pound sign needed)  
 5th line: #brief description of code/method (pound sign needed)  
 6th line: #other info about the case, such as spatial accuracy (pound sign needed)  
 7th line: #other info about the case, such as turb model (pound sign needed)  
 8th line: #other info about the case (pound sign needed)  
 9th line: variables="x/c","Cf"  
 10th line: zone t="surface Cf, no flow case"  
 subsequent lines: x/c Cf <- this is the data for no flow case  
 next line: zone t="surface Cf, suction case"  
 subsequent lines: x/c Cf <- this is the data for suction case

The sample datafile case3.cf.SAMPLE.dat can be downloaded from the websit

c. Velocity profiles and turbulence data at several stations along the lower wall for no-flow and suction cases. For time-accurate computations, these should be the long-time-averaged profiles. The 15 required stations are:  $x/c=-2.14, 0, .2, .4, .65, .66, .8, .9, 1.0, 1.1, 1.2, 1.3, 1.4, 1.6, 2.0$ . The profiles should be taken along a VERTICAL line at each given x-location (not necessarily normal to the hump surface), extending from the wall up to at least past the boundary layer and/or separation bubble. Also, if your computations included the inside of the slot, include profiles along one line at  $x=0.647$  inside the slot (from the lower wall to the upper wall, y goes from approximately 0.1105 to 0.1142 at this x location). Submit the following quantities:  $u/U_{inf}$ ,  $u'u'bar/U_{inf}^2$ ,  $v'v'bar/U_{inf}^2$ , and  $u'v'bar/U_{inf}^2$ , where:

$u$  = horizontal velocity component  
 $v$  = vertical velocity component  
 $u'u'bar$  = turbulent normal stress in horizontal direction (optional)  
 $v'v'bar$  = turbulent normal stress in vertical direction (optional)  
 $u'v'bar$  = turbulent shear stress in x-y plane

Submit two separate files, one for no-flow-control, and one for constant suction. Name these files: case3.pro.noflow.ANYTHING.dat case3.pro.suction.ANYTHING.dat-where "ANYTHING" can be any descriptor you choose (should be different for each file if you are submitting multiple runs)-the file should be in 7-column format:

1st line: #your name (pound sign needed)  
 2nd line: #your affiliation (pound sign needed)  
 3rd line: #your contact info (pound sign needed)  
 4th line: #brief description of grid (pound sign needed)  
 5th line: #brief description of code/method (pound sign needed)  
 6th line: #other info about the case, such as spatial accuracy (pound sign needed)  
 7th line: #other info about the case, such as turb model (pound sign needed)  
 8th line: #other info about the case (pound sign needed)  
 9th line: variables="x/c","y/c","u/Uinf","v/Uinf","uu/Uinf^2",  
 "vv/Uinf^2","uv/Uinf^2"  
 10th line: zone t="x/c=-2.14"

subsequent lines:  $x/c$   $y/c$   $u/U_{inf}$   $v/U_{inf}$   $uu/U_{inf}^2$   $vv/U_{inf}^2$   $uv/U_{inf}^2$  <- this is the data at  $x/c=-2.14$   
next line: zone  $t="x/c=0"$   
subsequent lines:  $x/c$   $y/c$   $u/U_{inf}$   $v/U_{inf}$   $uu/U_{inf}^2$   $vv/U_{inf}^2$   $uv/U_{inf}^2$  <- this is the data at  $x/c=0$   
next line: zone  $t="x/c=0.2"$   
subsequent lines:  $x/c$   $y/c$   $u/U_{inf}$   $v/U_{inf}$   $uu/U_{inf}^2$   $vv/U_{inf}^2$   $uv/U_{inf}^2$  <- this is the data at  $x/c=0.2$   
next line: zone  $t="x/c=0.4"$   
subsequent lines:  $x/c$   $y/c$   $u/U_{inf}$   $v/U_{inf}$   $uu/U_{inf}^2$   $vv/U_{inf}^2$   $uv/U_{inf}^2$  <- this is the data at  $x/c=0.4$   
next line: zone  $t="x/c=0.65"$   
subsequent lines:  $x/c$   $y/c$   $u/U_{inf}$   $v/U_{inf}$   $uu/U_{inf}^2$   $vv/U_{inf}^2$   $uv/U_{inf}^2$  <- this is the data at  $x/c=0.65$   
next line: zone  $t="x/c=0.66"$   
subsequent lines:  $x/c$   $y/c$   $u/U_{inf}$   $v/U_{inf}$   $uu/U_{inf}^2$   $vv/U_{inf}^2$   $uv/U_{inf}^2$  <- this is the data at  $x/c=0.66$   
next line: zone  $t="x/c=0.8"$   
subsequent lines:  $x/c$   $y/c$   $u/U_{inf}$   $v/U_{inf}$   $uu/U_{inf}^2$   $vv/U_{inf}^2$   $uv/U_{inf}^2$  <- this is the data at  $x/c=0.8$   
next line: zone  $t="x/c=0.9"$   
subsequent lines:  $x/c$   $y/c$   $u/U_{inf}$   $v/U_{inf}$   $uu/U_{inf}^2$   $vv/U_{inf}^2$   $uv/U_{inf}^2$  <- this is the data at  $x/c=0.9$   
next line: zone  $t="x/c=1.0"$   
subsequent lines:  $x/c$   $y/c$   $u/U_{inf}$   $v/U_{inf}$   $uu/U_{inf}^2$   $vv/U_{inf}^2$   $uv/U_{inf}^2$  <- this is the data at  $x/c=1.0$   
next line: zone  $t="x/c=1.1"$   
subsequent lines:  $x/c$   $y/c$   $u/U_{inf}$   $v/U_{inf}$   $uu/U_{inf}^2$   $vv/U_{inf}^2$   $uv/U_{inf}^2$  <- this is the data at  $x/c=1.1$   
next line: zone  $t="x/c=1.2"$   
subsequent lines:  $x/c$   $y/c$   $u/U_{inf}$   $v/U_{inf}$   $uu/U_{inf}^2$   $vv/U_{inf}^2$   $uv/U_{inf}^2$  <- this is the data at  $x/c=1.2$   
next line: zone  $t="x/c=1.3"$   
subsequent lines:  $x/c$   $y/c$   $u/U_{inf}$   $v/U_{inf}$   $uu/U_{inf}^2$   $vv/U_{inf}^2$   $uv/U_{inf}^2$  <- this is the data at  $x/c=1.3$   
next line: zone  $t="x/c=1.4"$   
subsequent lines:  $x/c$   $y/c$   $u/U_{inf}$   $v/U_{inf}$   $uu/U_{inf}^2$   $vv/U_{inf}^2$   $uv/U_{inf}^2$  <- this is the data at  $x/c=1.4$   
next line: zone  $t="x/c=1.6"$   
subsequent lines:  $x/c$   $y/c$   $u/U_{inf}$   $v/U_{inf}$   $uu/U_{inf}^2$   $vv/U_{inf}^2$   $uv/U_{inf}^2$  <- this is the data at  $x/c=1.6$   
next line: zone  $t="x/c=2.0"$   
subsequent lines:  $x/c$   $y/c$   $u/U_{inf}$   $v/U_{inf}$   $uu/U_{inf}^2$   $vv/U_{inf}^2$   $uv/U_{inf}^2$  <- this is the data at  $x/c=2.0$   
next line: zone  $t="inside slot, x/c=0.647"$   
subsequent lines:  $x/c$   $y/c$   $u/U_{inf}$   $v/U_{inf}$   $uu/U_{inf}^2$   $vv/U_{inf}^2$   $uv/U_{inf}^2$  <- this is the data inside slot at  $x/c=0.647$

The sample datafile [case3.pro.noflow.SAMPLE.dat](#) can be downloaded on the website

d. Field line-contour-plots (in one of the following formats: ps, eps, or jpg) of streamlines (average streamlines for time-accurate computations) for no-flow and suction cases. These plots should be black-and-white line plots only. The plots should go from approximately  $x/c=0.6$  to 1.6, and should contain enough streamlines to show the approximate size and shape of the separation bubble. The x-to-y ratio of the plot should be 1.0. The purpose of submitting these plots is to get a qualitative picture of the flowfields. Altogether, submit 2 plots files, one for the no-flow-control case and one for the steady suction case. Name these files:

case3.stream.noflow.ANYTHING.eps

case3.stream.suction.ANYTHING.eps

(where the "eps" in this case means encapsulated postscript - use ps, or jpg instead if appropriate).

e. (For optional condition 3 only)  $x/c$  vs. long-time-averaged  $C_p$  on the lower wall for oscillatory case. Include results at least as far upstream as  $x/c=-2.14$ , and at least as far downstream as  $x/c=2.0$ . Do not include the data on the walls deep inside the slot. Name this file: case3.cposc.ANYTHING.dat-where "ANYTHING" can be any descriptor you choose (should be different for each file if you are submitting multiple runs) -the file should be in 2-column format:

1st line: #your name (pound sign needed)

2nd line: #your affiliation (pound sign needed)

3rd line: #your contact info (pound sign needed)

4th line: #brief description of grid (pound sign needed)

5th line: #number of time steps per cycle (pound sign needed)

6th line: #brief description of code/method (pound sign needed)

7th line: #other info about the case, such as spatial accuracy (pound sign needed)

8th line: #other info about the case, such as turb model (pound sign needed)

9th line: #other info about the case (pound sign needed)

10th line: variables=" $x/c$ ", " $C_p$ "

11th line: zone t="surface  $C_p$ , oscillatory case"

subsequent lines:  $x/c$   $C_p$  <- this is the data for oscillatory case

The sample datafile case3.cposc.SAMPLE.dat can be downloaded on the website



# CASE 3: DIRECT NUMERICAL SIMULATION ON THE CRAY X1

D. Postl<sup>1</sup>, S. Wernz<sup>1</sup>, and H. F. Fasel<sup>1</sup>

<sup>1</sup>*Department of Aerospace and Mechanical Engineering, The University of Arizona, Tucson, AZ 85721*

## Introduction

In the present approach, we assess the feasibility of simulating complex flows at high Reynolds numbers without the use of turbulence models. With the ever-increasing availability of computational resources on supercomputers such as the Cray X1, it has become possible to perform three-dimensional computations using hundreds of millions of grid points. Despite the fact that such high Reynolds number simulations may not be fully resolved all the way down to the smallest scales, they are considered to be useful for studying the development and the dynamics of large coherent structures in complex turbulent flows as well as for aiding in our interpretation of results obtained from turbulence models.

## Solution Methodology

The computer code that was used for the present simulations is based on a highly accurate incompressible Navier-Stokes solver developed for investigating transitional and turbulent boundary layer flows [1]. While the original code was written for a Cartesian grid, it has since been adapted to orthogonal curvilinear coordinates [2]. In the code, the 3D Navier-Stokes equations are solved in vorticity-velocity formulation. This formulation of the governing equations is obtained by taking the curl of the momentum equation, thus eliminating the pressure term. Taking into consideration the fact that both velocity and vorticity vectors are solenoidal and using the following definition for the vorticity,

$$\boldsymbol{\omega} = -\nabla \times \mathbf{v}, \quad (1)$$

the vorticity transport equation

$$\frac{\partial \boldsymbol{\omega}}{\partial t} + (\mathbf{v} \cdot \nabla) \boldsymbol{\omega} - (\boldsymbol{\omega} \cdot \nabla) \mathbf{v} = \frac{1}{Re} \nabla^2 \boldsymbol{\omega} + \nabla \times \mathbf{F} \quad (2)$$

is obtained. The velocity field,  $\mathbf{v}$ , is obtained from the vorticity,  $\boldsymbol{\omega}$ , through the vector Poisson equation

$$\nabla^2 \mathbf{v} = \nabla \times \boldsymbol{\omega}. \quad (3)$$

The governing equations are non-dimensionalized using a reference velocity  $U_{ref}$  (e.g. free stream velocity  $U_\infty$ ) and a reference length  $L_{ref}$  (e.g. cord length  $c$ ). The volume force,  $\mathbf{F}$ , on the right-hand-side of Eq. (2) will be discussed in the next section.

For the time-integration of the vorticity-transport equations, a four-stage explicit Runge-Kutta scheme with fourth-order accuracy is employed. For the spatial discretization, fourth-order compact differences are used in the streamwise and in the wall-normal directions. Assuming periodicity in the spanwise direction ( $z$ ), a pseudo-spectral approach is taken. Each variable is represented by a total of  $2K+1$  Fourier modes: the 2-D spanwise average (zeroth Fourier mode),  $K$  symmetric Fourier cosine as well as  $K$  anti-symmetric Fourier sine modes. As a result of this decomposition, the 3D governing equations reduce to a set of 2D equations for each Fourier mode.

The equations for the velocity components, Eq. (3), can be reduced to a set of 2 ODEs (for the stream-wise and spanwise velocity components) and, as a result of the transformation to orthogonal curvilinear coordinates, a 2D convection-diffusion equation with variable coefficients for the wall-normal velocity component (for each Fourier mode). This equation is of the form

$$\frac{\partial^2 v}{\partial \xi^2} + \alpha(\xi, \eta) \cdot \frac{\partial^2 v}{\partial \eta^2} + \beta(\xi, \eta) \cdot \frac{\partial v}{\partial \xi} + \gamma(\xi, \eta) \cdot \frac{\partial v}{\partial \eta} + \delta(\xi, \eta) \cdot v = f(\xi, \eta) \quad (4)$$

and its solution represents the single most computationally expensive step in the numerical integration of the governing equations. Eq. (4) is discretized using a fourth-order accurate nine-point stencil. The derivation of this stencil is based on an extension to the procedure described in [4]. The resulting linear system is solved iteratively using a zebra-alternating-line Gauss-Seidel (ZALGS) algorithm with multigrid acceleration. Despite its slightly inferior smoothing properties compared to the incomplete-line-LU-decomposition algorithm, the ZALGS was chosen because it can easily be vectorized.

The code has been parallelized using the Message Passing Interface (MPI). The parallelization is done in the spanwise direction because the solution of Eq. (4) greatly complicates an efficient implementation of typical domain decomposition techniques. Using the present domain decomposition with respect to the Fourier modes only yields good parallel efficiency on supercomputers with extremely high communication bandwidths. This is due to the fact that the computation of the non-linear terms in the vorticity transport equations is done in physical space. The vectorized FFT routines require data to be local to each process, which necessitates swapping of the entire 3D arrays before and after each time the flow field is transformed from spectral to physical space and vice versa. The Cray X1, with its communication bandwidth of 10 GB/s, allows for this task to be performed in a short time compared to the computation of the FFTs.

## Implementation and Case Specific Details

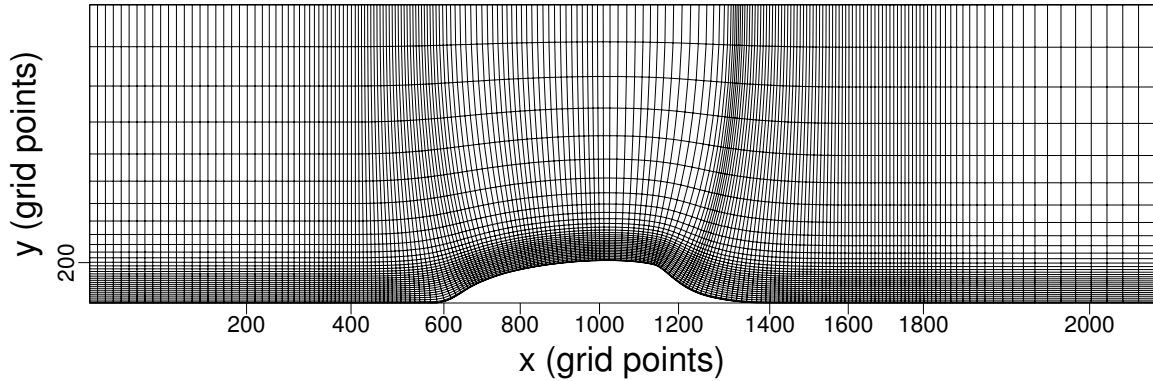


Figure 1: Computational grid. Every  $10^{th}$  point shown in both  $x$  and  $y$ .

The grid used for the simulations is shown in Fig. 1. It was obtained from an iterative solver that was developed to generate orthogonal curvilinear grids based on the method described in [5]. At each step of the iteration, the following set of equations,

$$\frac{\partial}{\partial \xi} \left( g \frac{\partial x_i}{\partial \xi} \right) + \frac{\partial}{\partial \eta} \left( \frac{1}{g} \frac{\partial x_i}{\partial \eta} \right) = 0, \quad i = 1, 2, \quad (5)$$

is solved using a multigrid algorithm similar to the one used in the Navier-Stokes code. The distribution of boundary points is obtained from a Newton-Raphson sub-iteration. The only control over grid point clustering is given by appropriate specification of the distortion function  $g$ . The grid generator was vectorized and

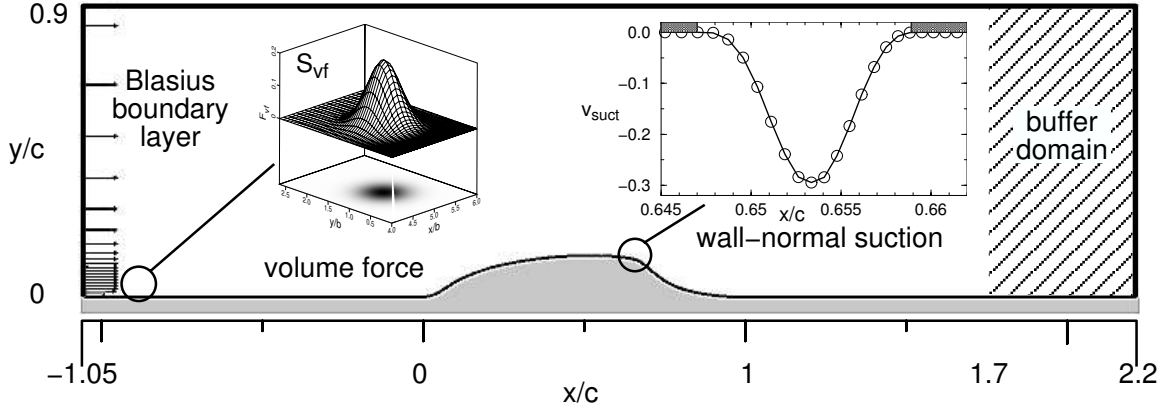


Figure 2: Sketch of computational domain.

domain size ( $\Delta X/c, \Delta Y/c, \Delta Z/c$ ):	3.25 , 0.9 , 0.071
number of grid points in $x, y$ :	2049, 321
number of non-symmetric Fourier modes in $z$ (K):	49
number of points in $z$ (for computing non-linear terms):	160
total number of points:	$\sim 105 \cdot 10^6$
$\Delta x^+, \Delta y^+, \Delta z^+$ (based on $x/c = -0.5$ ):	27 ... 92, 1.2, 17
$\Delta t \cdot U_\infty/c$ (condition 1)	$3.3 \cdot 10^{-4}$
$\Delta t \cdot U_\infty/c$ (condition 2)	$1.4 \cdot 10^{-4}$

Table 1: Computational parameters.

ported to the Cray X1 because, in order to obtain a high-quality orthogonal grid, Eqs. (5) need to be solved hundreds of thousands of times.

An illustration of the computational domain for the Navier-Stokes simulations is given in Fig. 2. At the inflow boundary,  $x/c = -1.05$ , a laminar Blasius boundary layer profile is imposed with  $Re_x = 22.6 \cdot 10^6$ . All velocity and vorticity components are prescribed as Dirichlet conditions. For maintaining the fourth-order accuracy of the code, the streamwise derivatives are prescribed as well. To prevent reflections from the outflow boundary, turbulent fluctuations are damped out in a buffer domain starting at  $x/c = 1.7$  using the approach discussed by Meitz and Fasel [1]. At the upper boundary, a slip-wall is imposed,  $v = 0$ , and irrotational flow is assumed,  $\omega = 0$ . Since the equations for the streamwise ( $u$ ) and spanwise ( $w$ ) velocity components reduce to ODEs in the streamwise direction, no upper boundary conditions are required for these quantities. At the wall, no-slip and no-penetration conditions are imposed, except over the suction slot at  $x/c \approx 0.65$ . The spanwise and streamwise vorticity components at the wall are obtained through forward integration by using the known velocity field at the new time level. The wall-normal vorticity component is set to zero everywhere except over the suction slot where its value is known from the boundary conditions on the velocities. Periodicity is assumed in the spanwise direction with the domain width chosen as  $\Delta Z/c = 0.071$ . This seemingly narrow domain was chosen as a compromise to achieve a reasonable spanwise resolution. The choice was also based on the authors' conviction that the coherent structures present in this flow are predominantly two-dimensional in nature. The relevant computational parameters are summarized in table 1.

The laminar boundary layer is tripped to turbulence near the inflow boundary (see Fig. 2) by introducing high-amplitude, 3D disturbances into the flow using a volume forcing technique, i.e. by adding a time-harmonic forcing term,  $\nabla \times \mathbf{F}_{vf}$ , to the right-hand-side of the vorticity transport equations (2). The force is

applied for selected spanwise Fourier components,  $k$ . For each of these  $k$ , it takes on the form of

$$\mathbf{F}_{vf}^{(k)}(\xi, \eta, k, t) = \sum_{n=1}^N \mathbf{A}_{vf}^{(n,k)} \cos(2\pi f^{(n,k)}t + \theta_{vf}^{(n,k)}) S_{vf}^{(n,k)}(\xi, \eta), \quad (6)$$

where vector  $\mathbf{A}_{vf}^{(n,k)} = (A_\xi, A_\eta, A_z)$  determines the amplitude and spatial orientation of the force, and  $f^{(n,k)}$  and  $\theta_{vf}^{(n,k)}$  are the frequency and phase angle in time. The spatial distribution of the volume force,  $S_{vf}^{(n,k)}$ , has the Gaussian shape

$$S_{vf}^{(n,k)} = \exp \left[ - \left( \frac{\xi - \xi_{vf}^{(n,k)}}{a_{vf}^{(n,k)}} \right)^2 - \left( \frac{\eta - \eta_{vf}^{(n,k)}}{b_{vf}^{(n,k)}} \right)^2 \right], \quad (7)$$

with  $a_{vf}^{(n,k)}$  and  $b_{vf}^{(n,k)}$  determining its size. The wall-normal forcing locations were chosen such as to achieve maximum receptivity of the flow to the disturbance input. Due to the forcing, the flow transitions to turbulence and at approximately  $x/c = -0.5$ , a fully developed turbulent profile is reached.

As a result of the tripping procedure described above, it was found to be difficult to precisely match a particular turbulent profile at a given streamwise location. Due to the limitations on available computational resources, it was impossible to trip a laminar boundary layer, match the given turbulent profile at  $x/c = -2.14$  and continue the computation all the way to and beyond the hump. Since it was noted by Seifert and Pack [6] that, in their experiments, the thickness of the upstream boundary layer had only a minor effect on the flow field, it was deemed more important to reach a fully turbulent state upstream of the hump than to precisely match the experimental boundary layer. In the present simulations, the approach boundary layer is thinner than the one in the experiments.

For the case involving steady suction (condition 2), the slot was modeled by a boundary condition on the wall-normal velocity component,

$$v_{suct} = A_{suct} \cdot \left[ \cos \left( 2\pi \frac{s}{w_{slot}} \right) \right]^3, \quad (8)$$

where  $s$  represents the distance from the center of the slot along the body surface. The width of the slot,  $w_{slot}$ , was increased to obtain a reasonable spatial resolution (see Fig. 2). The strength of the suction,  $A_{suct} = -0.3$ , was adjusted accordingly to match the specified suction rate of 0.015 kg/s.

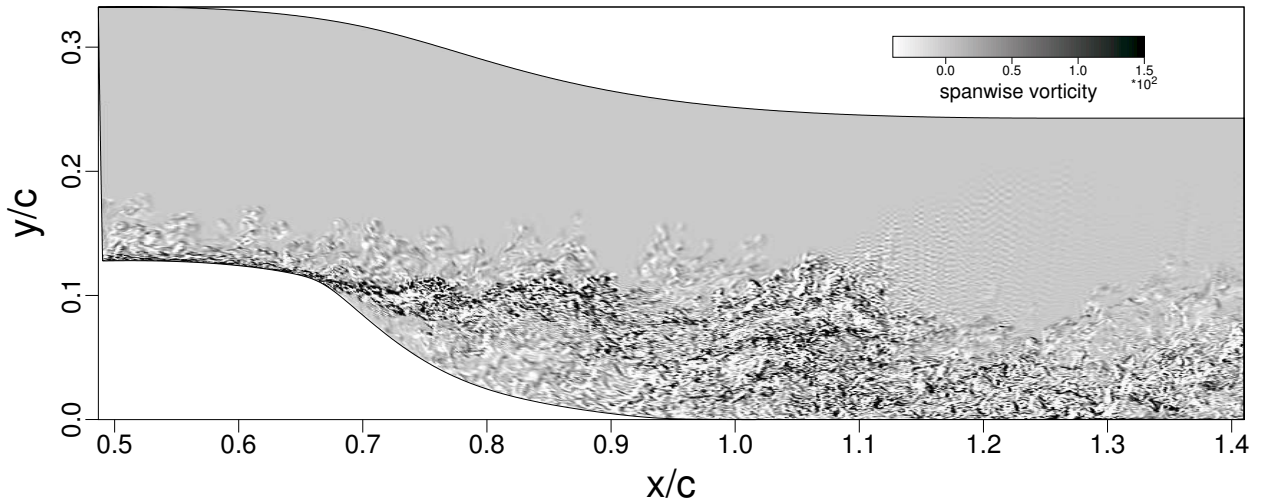


Figure 3: Instantaneous gray-scale contours of the spanwise vorticity. Unforced case.



Instantaneous gray-scale contours of the spanwise vorticity component are shown in Fig. 3 for the unforced case (condition 1) and in Fig. 4 for the case with steady suction (condition 2).

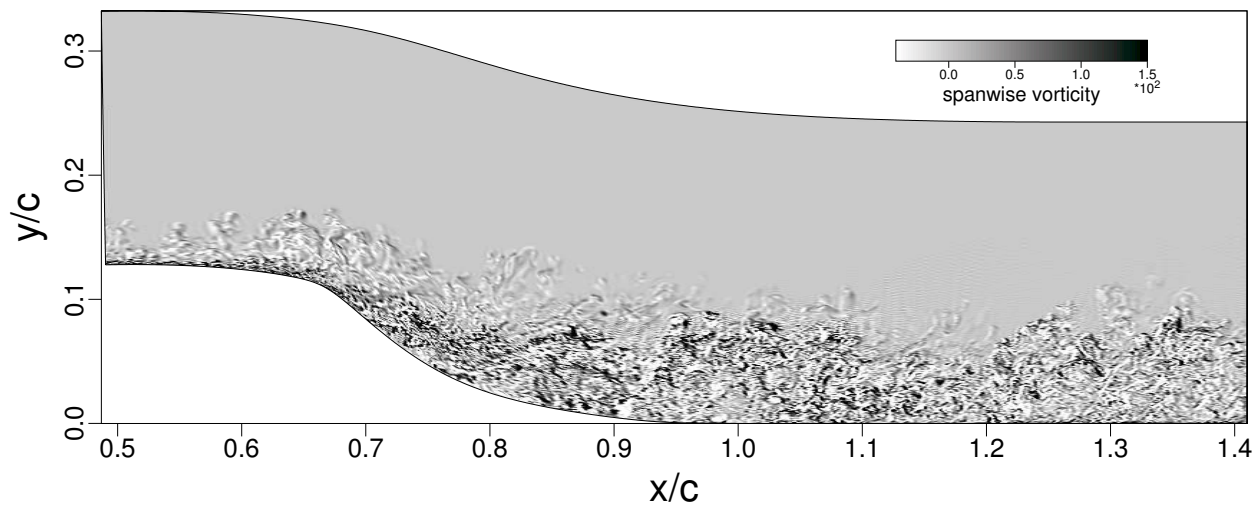


Figure 4: Instantaneous gray-scale contours of the spanwise vorticity. Case with steady suction.

## Acknowledgments

This work was supported by the Air Force Office of Scientific Research (AFOSR) under grant number F49620-02-1-0122, with Dr. Thomas J. Beutner serving as the program manager. Computing time on the Cray X1 at the Army High Performance Computing Research Center (AHPCRC) and at the US Army Engineer Research and Development Center (ERDC) is gratefully acknowledged.

## References

- [1] Meitz, H.L., Fasel, H.F. "A Compact-Difference Scheme for the Navier-Stokes Equations in Vorticity-Velocity Formulation" *J. Comp. Phys.* vol. 157, pp. 371–403, 2000.
- [2] Postl, D. *Dissertation*, University of Arizona, 2004.
- [3] Kloker, M., Konzelmann, U., Fasel, H. "Outflow Boundary Conditions For Spatial Navier-Stokes Simulations of Transitional Boundary Layers" *AIAA J.* vol. 31 (4), 1993
- [4] Dennis, S.C.R., Hudson, J.D. "Compact  $h^4$  Finite-Difference Approximations to Operators of Navier-Stokes Type" *J. Comp. Phys.* vol. 85, pp. 390–416, 1989.
- [5] Duraiswami, R., Prosperetti, A. "Orthogonal Mapping in Two Dimensions" *J. Comp. Phys.* vol. 98, pp. 254–268, 1992.
- [6] Seifert, A., Pack, L.G. "Active Flow Separation Control on Wall-Mounted Hump at High Reynolds Numbers" *AIAA J.* vol. 40 (7), 2002



## CASE 3: PREDICTION USING RANS AND DES

Vivek Krishnan<sup>1</sup>, Kyle D. Squires<sup>1</sup> and James R. Forsythe<sup>2</sup>

<sup>1</sup>MAE Department, Arizona State University, Tempe, AZ 85281-6106

<sup>2</sup>Cobalt Solutions, LLC, 4636 New Carlisle Pike, Springfield, OH 45504

### Introduction

The development of computational tools that can be used to guide technologies for flow control applications at realistic Reynolds numbers and in complicated configurations is a topic of significant interest. Computational Fluid Dynamics (CFD) offers a useful tool in understanding flow characteristics and studying the performance gains that can be achieved through flow control, though advances in several areas are needed to improve the robustness of CFD predictions for applications.

Most of the flow fields for which control would be advantageous are often very complex – the flows are far from equilibrium, e.g., separated or on the verge of separation, and distorted by effects such as strong pressure gradients and streamline curvature. Application Reynolds numbers are sufficiently high that empirical input to any simulation strategy appears unavoidable. In addition, it would be desirable in many flow control applications to exert a “microscopic” (e.g., small-scale) input and observe a desired “macroscopic” (large-scale) output. This implies a wide range in the geometric scales to be simulated, which in turn places significant burdens on issues such as grid design and construction, possibly more so than in most conventional CFD applications. Thus, the opportunity for a thorough assessment of simulation strategies against measurements and other simulation approaches represents a valuable undertaking. Summarized in this report are predictions of Case 3 using solutions of the Reynolds-averaged Navier-Stokes (RANS) equations and Detached-Eddy Simulation (DES).

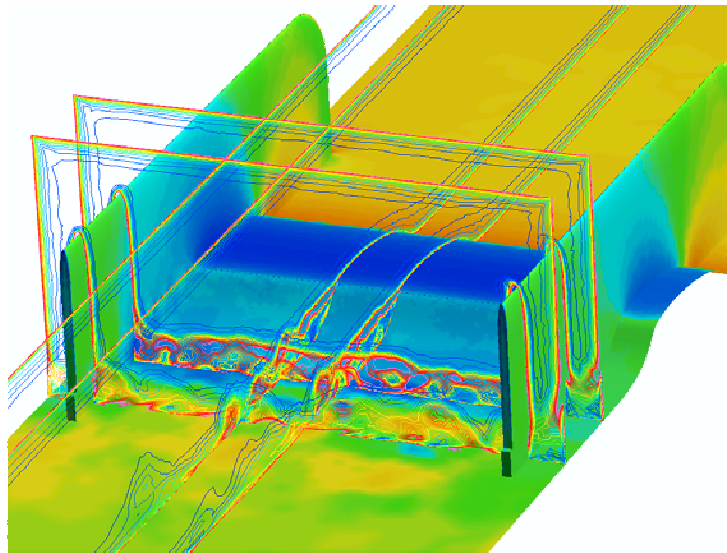


Figure 1: Contours of the instantaneous vorticity magnitude in the leeward region of hump. Flow field prediction of the no-flow-control case obtained using DES. Surfaces colored by pressure.

## Solution Methodology

The compressible Navier-Stokes equations are solved using *Cobalt*. The numerical method is a cell-centered finite volume approach applicable to arbitrary cell topologies (e.g, hexahedra, prisms, tetrahedra) and described in Strang *et al.*[1]. The spatial operator uses the exact Riemann Solver of Gottlieb and Groth [2], least-squares gradient calculations using QR factorization to provide second order accuracy in space, and TVD flux limiters to limit extremes at cell faces. A point implicit method using analytic first-order inviscid and viscous Jacobians is used for advancement of the discretized system. For time-accurate computations, a Newton sub-iteration scheme is employed, the method is second order accurate in time. The domain decomposition library ParMETIS [3] is used for parallel implementation and provides optimal load balancing with a minimal surface interface between zones. Communication between processors is achieved using Message Passing Interface.

## Model Description

Summarized in the next section are the simulation parameters for both two-dimensional (2D) and three-dimensional (3D) configurations using RANS and DES. RANS predictions are obtained using two turbulence models: the Spalart-Allmaras one-equation model [4] (referred to as S-A throughout) and the two-equation SST model of Menter [5]. All of the calculations summarized below are of fully turbulent flows, i.e., with turbulent boundary layers initiated along all solid surfaces of the computational domain.

The DES formulation is obtained by replacing in the S-A model the distance to the nearest wall,  $d$ , by  $\tilde{d}$ , where  $\tilde{d}$  is defined as,

$$\tilde{d} \equiv \min(d, C_{DES}\Delta), \quad C_{DES} = 0.65. \quad (1)$$

In Eq. (1),  $\Delta$  is the largest distance between the cell center under consideration and the cell center of the neighbors (i.e., those cells sharing a face with the cell in question). The location where  $\tilde{d}$  is determined by the grid spacing, i.e.,  $\tilde{d} = C_{DES}\Delta$ , defines the interface between the RANS region and the LES region. In applications for which the wall-parallel grid spacings (e.g., streamwise and spanwise) are on the order of the boundary layer thickness, the RANS region comprises most or all of the boundary layer and the closure applied is the S-A RANS model. In the LES region the closure is a one-equation model for the subgrid scale eddy viscosity. For the present configuration, the combination of the adverse pressure gradient upstream of the hump thickened the boundary layer. That feature combined with the spacings for the current grids caused the RANS-LES interface to reside sufficiently within the boundary layer such that the upstream flow prediction was less accurate compared to RANS results and experimental measurements. To provide an evaluation of the DES predictions against the RANS for nominally similar upstream conditions, RANS behavior was maintained to  $x/C = 0.65$ , slightly upstream of the slot ( $C$  is the hump chord length).

## Implementation and Case Specific Details

All of the computations to be reported at the workshop are summarized in Tables 1-3. The table reports the grid sizes, grid topology, whether the computation was 2D or 3D, the boundary conditions, and turbulence models employed for a given simulation (the “X” in the table indicating the simulation was performed). The nomenclature in the tables for the grid topology indicates whether the mesh was structured or unstructured and with additional details for the 3D computations as summarized below. The nomenclature for the boundary conditions “slip top wall” indicates a slip condition was applied to the upper surface of the computational domain, “bl top wall” indicates a boundary layer grid on the top wall and that the no-slip condition was applied, and “bl all walls” indicates boundary layer grids on all walls and the imposition of no-slip conditions on all solid surfaces. The distance from the lower horizontal surfaces (that are faired to the upstream and downstream sides of the hump) to the upper boundary of the computational domain was 15.032 inches (slightly less than one chord length).

	grid size	grid topology	boundary conditions	RANS		DES S-A
				S-A	SST	
2D	$421 \times 109$	structured	slip top wall	X	X	
	$841 \times 101$	structured	slip top wall	X	X	
	$841 \times 217$	structured	slip top wall	X	X	
	$841 \times 257$	structured	slip top wall	X		
	$841 \times 257$	structured	bl top wall	X		
	$890 \times 257$	structured	bl top wall	X		
	$1.14 \times 10^5$	unstructured	slip top wall	X		
	$2.47 \times 10^5$	unstructured	slip top wall	X		
3D	$841 \times 101 \times 41$	structured, periodic	slip top wall			X
	$2.59 \times 10^6$	unstructured, half-geometry	bl all walls	X		
	$4.90 \times 10^6$	unstructured, half-geometry	bl all walls	X	X	
	$10.72 \times 10^6$	unstructured, half-geometry	bl all walls	X		
	$9.14 \times 10^6$	unstructured, full-geometry	bl all walls			X

Table 1: Summary of the computations of the no-flow-control case.

Parameters summarized in the tables correspond to three sets of calculations. The predictions of the “no-flow-control” case in Table 1 were performed using configurations that meshed the cavity and slot, though with the lower (horizontal) cavity surface closed. The steady-suction case imposed a fixed mass flux of 0.01518 kg/s (divided by the 23 inch span of the slot through which suction was applied in the experiments) along the entire lower cavity surface. The zero-net-mass-flux oscillatory suction/blowing was performed by prescribing a sinusoidal variation in the mass flux exiting/entering the lower cavity surface. The suction/blowing frequency was that prescribed on the workshop web page, i.e., 138.5 Hz. The peak mass flux was adjusted at the lower cavity surface in order that the maximum velocity out of the slot was approximately 26.6 m/s, which corresponded to a mass flux of 0.0179 kg/s (over the entire slot) as summarized in Table 3. As also shown in Table 3, additional suction/blowing rates were applied in order to investigate the characteristics of the jet velocity through the slot and impedance effects associated with large blowing coefficients. The results from these simulations will be presented at the workshop, though are not included with the data files that were submitted.

For each simulation, the reference conditions corresponded to standard atmosphere. At the outlet of the computational domain the pressure was prescribed at 14.696 psia, the reference temperature was 519 Rankine, and the corresponding density specified using the ideal gas law. The reference Mach number was 0.1, leading to a Reynolds number per unit of length of  $5.899 \times 10^4$ , which yields a chord-based Reynolds number of  $9.75 \times 10^5$  for the simulations summarized below. For the 2D simulations the reference pressure used in calculation of the pressure coefficient was adjusted in order to match experimental measurements upstream of the hump leading edge. For the 3D calculations the pressure coefficient was computed using the reference conditions in the freestream at  $x/C = -2.14$  (the coordinate origin  $x/C = 0$  corresponding to the hump leading edge).

Additional notes on the 2D cases:

1. RANS calculations were performed on two of the 2D structured grids available on the workshop web site and on two of the 2D unstructured grids available on the workshop web site. The 2D structured grids comprised of  $841 \times 217$  cells and  $421 \times 109$  cells are referred to as “Structured 2D Grid #1” and “Structured 2D Grid #2” on the web site. The unstructured grids comprised of  $2.45 \times 10^5$  cells and  $1.12 \times 10^5$  cells are referred to as “Unstructured 2D Grid #1” and “Unstructured 2D Grid #2” on the web site.
2. The structured grid comprised of  $841 \times 101$  cells was created using Gridgen, and starting with the “Structured 2D Grid #1”. The grid resolution was coarsened in the wall normal direction, while the

	grid size	grid topology	boundary conditions	RANS		DES S-A
				S-A	SST	
2D	$421 \times 109$	structured	slip top wall	X	X	
	$841 \times 101$	structured	slip top wall	X	X	
	$841 \times 217$	structured	slip top wall	X	X	
3D	$841 \times 101 \times 41$	structured, periodic	slip top wall			X
	$4.90 \times 10^6$	unstructured, half-geometry	bl all walls	X	X	

Table 2: Summary of the computations of the steady-suction case.

	grid size	grid topology	boundary conditions	RANS S-A	mass flux (kg/s)
2D	$841 \times 101$	structured	slip top wall	X	0.0179
	$841 \times 101$	structured	slip top wall	X	0.0140
	$841 \times 101$	structured	slip top wall	X	0.0210
	$841 \times 101$	structured	slip top wall	X	0.0280
	$841 \times 101$	structured	slip top wall	X	0.0560

Table 3: Summary of the computations of the pulsed blowing and suction case.

surface point distribution was left unchanged. The first  $y$ -location off the wall was also unchanged. This grid was created in order to provide a more efficient mesh for subsequent DES calculations that extruded this grid into the span.

3. With the exception of the 2D RANS calculation of the baseline case using the grid comprised of  $890 \times 257$  cells, the upstream section of the computational domain extended 6.39 chords forward of the hump leading edge. The simulation domain for the case with the grid size  $890 \times 257$  extended 10.64 chord lengths upstream of the leading edge. The purpose of the computation was to investigate the influence of thicker upper-wall boundary layer on the pressure distribution over the lower surface (on which the hump is mounted). Along the lower surface of the domain from 10.64 to 6.39 chord lengths a slip condition was applied, with a no-slip condition applied at the streamwise location 6.39 chord lengths upstream of the hump leading edge. This in turn allowed the boundary layer to develop from the same upstream location as the other simulations.
4. The downstream section of the domain for all 2D computations extended three chord lengths from the trailing edge of the hump.
5. With the exception of the simulations performed of the case with pulsed suction/blowing (c.f., Table 3), all RANS predictions are of the steady state flow. The governing equations were integrated using large timesteps, corresponding to a  $CFL = 10^6$ .
6. The predictions of the pulsed suction/blowing case were time-accurate. Based on the results of a timestep study, the timestep non-dimensionalized by the hump chord length and freestream velocity (computed using the reference Mach number of 0.1 and reference temperature) was  $8 \times 10^{-4}$  ( $1 \times 10^{-5}$  seconds). The mass flux values in Table 3 correspond to the peak values (divided by the 23 inch span of the slot).

Additional notes on the 3D cases:

1. All DES predictions were of the unsteady flow using time-accurate computations. A timestep study was performed using the DES of the baseline configuration (no flow control) and the grid comprised

of  $841 \times 101 \times 41$  cells. Dimensional timesteps of  $2 \times 10^{-5}$ ,  $4 \times 10^{-5}$ , and  $8 \times 10^{-5}$  seconds (corresponding to dimensionless values of 0.0016, 0.0032, and 0.0064) were employed in the calculations. Evaluation of frequency spectra at three locations in the separated region indicated relatively small differences in the spectra for simulations using timesteps of  $2 \times 10^{-5}$  and  $4 \times 10^{-5}$  seconds. Consequently, for the DES predictions summarized in Tables 1 and Table 2 the timestep was  $4 \times 10^{-5}$  seconds.

2. Tests of the time-dependent nature of the RANS flow fields were performed for a few select cases in which the RANS equations were integrated in a time-accurate fashion. These tests showed that the time-accurate RANS predictions evolved to steady solutions. Thus, the 3D RANS predictions summarized in the tables and to be presented at the workshop are of the steady state flow, obtained by integrating the equations using large timesteps, corresponding to a  $CFL = 10^6$ .
3. The DES prediction in Table 1 obtained using the structured grid was of a section of the hump. A grid with  $841 \times 101$  cells (and used in the RANS calculations as summarized in Tables 2 and 3) was extruded into the spanwise direction to create the 3D geometry. The spanwise dimension was meshed using 41 points with an equal spacing of 0.05 inches, leading to a spanwise period of 0.12 chord lengths. Periodic boundary conditions were applied along the spanwise direction, indicated by the reference “structured, periodic” in the grid topology entry in the tables.
4. Aside from the structured grid, the 3D computations summarized in Table 1 and Table 2 considered the entire tunnel geometry, i.e., from the splitter plate to the upper wall and spanwise extent of the lower test surface, including the endplates that are attached to the hump. The RANS predictions are of half the geometry with a symmetry condition imposed along the centerplane (indicated by the “half-geometry” entry in the tables). The DES prediction on the grid with  $9.14 \times 10^6$  cells is of the entire geometry, i.e., without any symmetry conditions imposed (indicated by the “full-geometry” entry in the tables). Contours of the instantaneous vorticity from the DES prediction are shown in Figure 1.

## Acknowledgments

The authors gratefully acknowledge the support of the Air Force Office of Scientific Research (Grant F49620-02-1-0117, Program Officer: Dr. Thomas Beutner). The computations were performed as part of a DoD Challenge project, on the Aeronautical Systems Major Shared Resource Center and the Maui High Performance Computing Center.

## References

- [1] Strang, W.Z., Tomaro, R.F. and Grismer, M.J., “The Defining Methods of Cobalt<sub>60</sub>: a Parallel, Implicit, Unstructured Euler/Navier-Stokes Flow Solver”, *AIAA 99-0786*, 1999.
- [2] Gottlieb, J.J. and Groth, C.P., “Assessment of Riemann solvers for unsteady one-dimensional inviscid flows of perfect gases”, *J. Comp. Physics*, Vol. 78, pp. 437-458, 1998.
- [3] Karypis, G., Schloegel, K., and Kumar, V, *ParMETIS: Parallel Graph Partitioning and Sparse Matrix Ordering Library Version 1.0*. University of Minnesota, Department of Computer Science, Minneapolis, MN 55455, July 1997.
- [4] Spalart, P.R. and Allmaras, S.R., “A One-Equation Turbulence model for Aerodynamic Flows”, *La Recherche Aerospatiale*, Vol. 1, pp. 5-21, 1994.
- [5] Menter, F.R., “Two-Equation Eddy-Viscosity Turbulence Models for Engineering Applications,” *AIAA Journal*, Vol. 32, No. 8, pp. 1598-1605, 1994.





# CASE 3: HIGH-ORDER HYBRID AND RANS SIMULATIONS OF A WALL-MOUNTED HUMP

P. E. Morgan<sup>1</sup>, D. P. Rizzetta<sup>2</sup>, and M. R. Visbal<sup>2</sup>

<sup>1</sup>*Ohio Aerospace Institute, Wright-Patterson, AFB, OH 45433*

<sup>2</sup>*Computational Sciences Branch, AFRL, Wright-Patterson, AFB, OH 45433*

## Introduction

The primary purpose of this study is to compare a high-order compact scheme with standard second-order methodologies for flow over a hump. The secondary purpose is to explore predictive capabilities of high-order hybrid techniques with those of standard Reynolds-Averaged Navier-Stokes (RANS) approaches.

## Solution Methodology

The governing equations are the unsteady, three-dimensional, full Navier-Stokes equations. The governing equations are expressed in general curvilinear coordinates and cast into strong conservation-law form. All dependent variables have been normalized by reference values except for  $p$ , which has been nondimensionalized by  $\rho_{ref} u_{ref}^2$ . Sutherland's law for the molecular viscosity coefficient  $\mu$  and the perfect gas relationship are also employed. Stokes' hypothesis has been invoked for the bulk viscosity coefficient.

Two forms of the above equations are implemented into the current scheme, the unfiltered and the Reynolds-averaged forms of the Navier-Stokes equations. The unfiltered form of the equations are employed for laminar, large eddy (LES) and direct numerical simulations (DNS). Standard compressible LES approaches use Favre-filtered Navier-Stokes equations, which result in additional subgrid-scale stress and heat flux terms that must be modeled with subgrid-scale (SGS) models. The present approach, referred to as the implicit LES (ILES) methodology, uses the unfiltered form of the equations and the scheme's filter in lieu of a SGS model to prevent pile up of energy at the high-wave numbers of the mesh. Classical Reynolds averaged simulations (RANS) are used to account for turbulence effects through the incorporation of an eddy viscosity model. The two-equation  $k - \epsilon$  model has been employed to compute the eddy viscosity. To better improve flow simulations in separated flow regions the  $k - \epsilon$  model has been modified to blend between the RANS model and the ILES approach. Hereafter this is referred to as the high-order hybrid approach.

## Time Integration

The solver advances the solution with second-order temporal accuracy using an implicit, subiterative Beam-Warming algorithm [1]. The approximate-factorization form of the Beam-Warming algorithm [1] may be written in delta form as

$$\begin{aligned} & \left[ I + \left( \frac{2\Delta t}{3} \right) \delta_{\xi 2} \left( \frac{\partial F^p}{\partial Q} - \frac{1}{Re} \frac{\partial F_v^p}{\partial Q} \right) \right] \times \left[ I + \left( \frac{2\Delta t}{3} \right) \delta_{\eta 2} \left( \frac{\partial G^p}{\partial Q} - \frac{1}{Re} \frac{\partial G_v^p}{\partial Q} \right) \right] \times \\ & \left[ I + \left( \frac{2\Delta t}{3} \right) \delta_{\zeta 2} \left( \frac{\partial H^p}{\partial Q} - \frac{1}{Re} \frac{\partial H_v^p}{\partial Q} \right) \right] \Delta Q = - \left( \frac{2\Delta t}{3} \right) \left[ \left( \frac{1}{2\Delta t} \right) (3Q^p - 4Q^n + Q^{n-1}) \right. \\ & \left. + \delta_{\xi 6} \left( F^p - \frac{1}{Re} F_v^p \right) + \delta_{\eta 6} \left( G^p - \frac{1}{Re} G_v^p \right) + \delta_{\zeta 6} \left( H^p - \frac{1}{Re} H_v^p \right) \right]. \end{aligned} \quad (1)$$

where  $\partial[F]/\partial Q$ ,  $\partial[G]/\partial Q$ , and  $\partial[H]/\partial Q$ , are flux Jacobians,  $Q$  is the solution vector, and  $\delta$  represents the spatial difference operator. Newton-like subiterations are incorporated to reduce linearization and factorization errors thereby improving the temporal accuracy and stability properties of the algorithm. Subiterations also permit the use of the more efficient diagonal form [2] of the implicit algorithm while retaining time accuracy. The subiterations are given by  $\Delta Q = Q^{p+1} - Q^p$  where  $p$  denotes the number of subiterations. For the first solver application ( $p = 1$ ),  $Q^p = Q^n$ , where  $n$  is the solution time-level. With subsequent subiterations  $Q^{p+1} \rightarrow Q^{n+1}$ . Based on previous unsteady flow computations, three applications of the solver per time step are typically found to be sufficient in order to recover second-order time accuracy.

The implicit portion of the algorithm uses second-order accurate three-point backward differencing for the time derivative and second-order central finite-difference approximations for the spatial derivatives (denoted with the subscript (2) in Eqn. 1. Nonlinear artificial dissipation (not shown) is appended to the implicit operator to enhance stability. Note that the spatial derivatives on the right-hand side of Eqn. 1 use high-order compact-difference operators (described below) that recover higher-order spatial accuracy with subiterations.

The  $k - \epsilon$  equations are solved uncoupled from the flow equations with a procedure similar to the one described above. Since the flow equations are solved uncoupled from the turbulence model, subiterations not only have the benefits described above, but also eliminate the time lag between the flow and turbulence model equations.

### **Spatial Discretization**

The governing equation spatial derivatives are discretized using the compact finite-difference scheme of Lele [3]. Using the tridiagonal subset of this scheme, the spatial derivative of any scalar  $f$ , such as a metric, flux component, or flow variable, can be obtained by solving the system:

$$\alpha \left( \frac{\partial f}{\partial \xi} \right)_{i-1} + \left( \frac{\partial f}{\partial \xi} \right)_i + \alpha \left( \frac{\partial f}{\partial \xi} \right)_{i+1} = a \left( \frac{f_{i+1} - f_{i-1}}{2} \right) + b \left( \frac{f_{i+2} - f_{i-2}}{4} \right) \quad (2)$$

where  $\alpha$ ,  $a$  and  $b$  determine the spatial properties of the algorithm. Of all the schemes this system generated, only the compact fourth-order scheme (C4), corresponding to  $\alpha = \frac{1}{4}$ ,  $a = \frac{3}{2}$ ,  $b = 0$ , was used in the present investigation.

Dispersion-error characteristics and truncation error of these schemes are discussed in detail in Refs. [3] and [4]. Also discussed in Ref. [4] are descriptions of the higher-order one-sided formulas used near boundaries.

### **Low-Pass Filter Scheme**

The non-dissipative compact difference scheme incorporated a non-dispersive spatial filter to eliminate numerical instabilities [5]. The filter is applied to the solution vector  $Q$  in each of the three computational directions following each subiteration. The filtered values of the solution vector are obtained by solving the tridiagonal system

$$\alpha_f \check{Q}_{i-1} + \check{Q}_i + \alpha_f \check{Q}_{i+1} = \sum_{n=0}^5 \frac{a_n}{2} (Q_{i+n} + Q_{i-n}) \quad (3)$$

where  $\check{Q}$  represents the filtered value of  $Q$ .  $\alpha_f$  is a free parameter for this family of filters which must remain in the range  $-0.5 \leq \alpha_f \leq 0.5$ . Higher values of  $\alpha_f$  correspond to less dissipative filters. The coefficients  $a_n$  in Eqn. 3 are summarized in Ref. [4]. On uniform meshes, these filters preserve constant functions, completely eliminate the odd-even mode decoupling, and do not amplify waves [6]. Low-pass filtering provides dissipation at the high modified wave numbers *only* where the spatial discretization already exhibits significant dispersion errors, whereas non-spectral based artificial viscosity and upwind-biased schemes introduce dissipation across a wide range of wavenumber.

Filtering of the first four points near any domain boundary requires the implementation of one-sided high-order Padé-type formulas as discussed in Refs. [4] and [5]. Unlike the interior filter, the one-sided high-order filters can amplify wave amplitudes for certain ranges of wavenumber. To eliminate this undesirable amplification behavior, higher values of  $\alpha_f$  are used near boundaries [8].

### **Parallelization and Multidomain Interface Treatment**

The above components are implemented in a parallel scheme based on an overset grid methodology. The overset grid implementation uses sixth-order explicit Lagrangian interpolation for the overlapping blocks. The overset grid methodology is used in conjunction with the MPI library for inter-block communication. The resulting MPI code has been successfully ported to several parallel platforms. Additional background on the parallel compact solver is covered in detail in Ref. [9].

### **Model Description**

The  $k - \epsilon$  model has been chosen to calculate the eddy viscosity,  $\mu_t$ , for RANS and high-order hybrid RANS/LES solutions. The Standard Jones and Launder model with the Low-Reynolds-Number corrections of Launder and Sharma [10] is employed as described in Ref. [11]. The  $k - \epsilon$  equations, like the flow equations, are also expressed in general curvilinear coordinates and conservation-law form. The current implementation varies from the standard model in the production term  $P_k$  which is now limited to prevent anomalous behavior in regions where the eddy viscosity should be near zero [11]. The term  $P_k$  is now given by

$$P_k = \min(P_k, 20.0\rho\epsilon) \quad (4)$$

where

$$P_k = \left(\frac{\mu_t}{Re}\right) \left(\phi - \frac{2}{3} \left(\frac{\partial u_k}{\partial x_k}\right)^2\right), \phi = |\omega| + 2 \min(0, |s| - |\omega|) \quad (5)$$

$|s|$  is the magnitude of the rate of strain tensor and  $|\omega|$  is the magnitude of the vorticity. This formulation reduces the eddy viscosity in regions of the flow where vorticity exceeds the rate of strain, such as in a vortex core, and has minimal effect in shear layers.

The high-order hybrid RANS/LES approach consists of two modifications to the  $k - \epsilon$  model described above. The first modification defines a new dissipation length scale for the  $k - \epsilon$  model based on the minimum grid cell size. The quantity  $[-\rho\epsilon]$  in the source term of the  $k$  equation is replaced with  $[-\frac{\rho k^{3/2}}{l}]$  where

$$l = \min(l_{k-\epsilon}, C\Delta), l_{k-\epsilon} = \frac{k^{3/2}}{\epsilon}, C = 0.61, \Delta = \max(\Delta s_x, \Delta s_y, \Delta s_z) \quad (6)$$

The second modification applies a double blending function which turns off the eddy viscosity away from the wall and in the separated flow region downstream of the hump. The blending function in the wall normal direction is given by

$$\mu_t = (1 - \Gamma)\mu_{t-RANS} + \Gamma\mu_{t-LES}, \Gamma = \tanh\left(\frac{d}{\alpha\lambda}\right)^2 \quad (7)$$

where  $\mu_{t-LES}$  is zero for the ILES approach,  $\lambda = k^{3/2}/\epsilon$ ,  $d$  is the distance to the nearest wall, and  $\alpha$  is a constant chosen such that  $\Gamma = 0.5$  in the log-law region for a flat plate boundary layer.

The streamwise blending function uses a sum of two hyperbolic tangent functions which rapidly turn off the eddy viscosity in the region between the downstream lip of the slot and  $x/c = 1.5$ . The total blending function is a product of the streamwise and normal blending functions.

Table 1: Case Summary

Case	Grid	Dimension	Scheme Order	Model	$\Delta\tau$	Span $z/c$	Flow Control		
							None	Suction	Oscillatory
1	Coarse	2D	2nd	RANS	$1.0 \times 10^{-4}$	n/a	x	x	x
2	Fine	2D	2nd	RANS	$5.0 \times 10^{-5}$	n/a	x	x	x
3	Coarse	2D	4th	RANS	$1.0 \times 10^{-4}$	n/a	x	x	x
4	Coarse	3D	2nd	RANS	$1.0 \times 10^{-4}$	0.36	x	x	
5	Coarse	3D	4th	RANS	$1.0 \times 10^{-4}$	0.36	x	x	
6	Coarse	3D	4th	HYBRID	$1.0 \times 10^{-4}$	0.13	x	x	

## Implementation and Case Specific Details

Multiple simulations were completed for this workshop which are summarized in Table 1. This study employed modified versions of the fine grid provided on the workshop website. The four-block mesh was reduced to a two-block mesh by eliminating the fourth block upstream of  $x/c = -2.14$  and by joining the second and third blocks which make up the slot and cavity used for flow control. The two-block grid was then smoothed while enforcing orthogonality at the walls with an elliptic solver. Finally, the slot mesh was extended five points into the hump grid to produce an overset topology. A coarse mesh was derived from this modified fine grid by eliminating every other point in each coordinate direction. For two-dimensional parallel calculations, the coarse mesh was divided into 19 blocks and the fine grid into 36 blocks.

Two three-dimensional meshes were also developed from the coarse 2D mesh. Both employed 51 points in the spanwise direction. The first 3D grid assumed symmetry at the span centerline so the half-span wind tunnel mesh had a  $\Delta z/c = 0.0139$ . The second mesh, used for periodic computations, employed a smaller span of approximately two boundary layer heights at the inflow corresponding to  $0.13304c$  which led to a  $\Delta z/c = 0.00289$ , when the periodic five-point overlap was removed. The 3D grid was partitioned into 56 blocks for the simulation.

Boundary conditions used in the simulations include adiabatic, no-slip walls for the lower surface of the wind tunnel, the hump, and walls of the slot. Inviscid wall boundary conditions were imposed for the top of the wind tunnel and the bottom of the cavity. For the no-suction case,  $v$  is set to zero at the bottom of the cavity. Similarly, suction and oscillatory blowing and suction cases are modeled by prescribing  $v$  at the base of the cavity to match the appropriate mass flow rate or slot velocity. Velocities and density are prescribed at the tunnel inflow, and pressure is updated with a Neumann boundary condition (i.e.  $\frac{\partial p}{\partial \xi} = 0$ ). This inflow profile, generated from a separate flat plate RANS calculation, matches the momentum thickness computed from the given experimental inflow profile. At the outflow, pressure is fixed and all other variables are updated using Neumann boundary conditions. For the two three-dimensional computations, symmetry and an inviscid wall boundary conditions are applied at the spanwise boundaries for the cases that model half the wind tunnel span, and periodicity is imposed in the spanwise direction of the second thin 3D mesh.

Due to the multiple parameters and cases being simulated, a single approach was not used to initialize the flow. In general, the two-dimensional coarse mesh cases initialized the hump domain with the inflow profile and specified no flow in the slot and cavity. The cavity pressure, density, and turbulence variables ( $k$ , and  $\epsilon$ ), were set to the wall values of the inflow profile. Since the coarse and fine grid locations are identical at every other grid point, the two-dimensional fine grid flow variables were initialized using the coarse grid solution at coincident grid points. The non-coincident mesh points were initialized by linearly interpolating the flow variables of surrounding points. Three-dimensional cases were initialized using the corresponding 2D solution for each spanwise plane.

The major findings of the study are

- The pressure coefficient was qualitatively correct for all cases. The peak magnitude was slightly

smaller than experimental values downstream of the hump mid-span and the separated flow region.

- Three-dimensional RANS simulations of the entire wind tunnel did not develop any appreciable span-wise flow variation.
- Preliminary computations with a Hybrid approach performed worse than the traditional RANS model.

## Acknowledgments

The authors are grateful for AFOSR sponsorship under task 2304IW monitored by Dr. T. Beutner. This work was also supported in part by grants of computer time from the DOD High Performance Computing Centers at ASC and NAVO.

## References

- [1] Beam, R.M. and Warming, R.F. "An Implicit Factored Scheme for the Compressible Navier-Stokes Equations," *AIAA J.*, Vol. 16, No. 4, pp.393-402, 1978.
- [2] Pulliam, T.H. and Chaussee, D.S. "A Diagonal Form of an Implicit Approximate-Factorization Algorithm," *J. of Computational Physics*, Vol. 39, No. 2, pp.347-363, 1981.
- [3] Lele, S.K. "Compact Finite Difference Schemes with Spectral-like Resolution," *J. of Computational Physics*, Vol. 103, pp.16-42, 1992.
- [4] Gaitonde, D.V. and Visbal, M.R. "High-Order Schemes for Navier-Stokes Equations:Algorithm and Implementation into FDL3DI," Air Force Research Labs Technical Report AFRL-VA-WP-TR-1998-3060, 1998.
- [5] Visbal, M.R. and Gaitonde, D.V. "High-Order Accurate Methods for Complex Unsteady Subsonic Flows," *AIAA J.*, Vol. 37, No. 10, pp.1231-1239, 1999.
- [6] Visbal, M.R. and Rizzetta, D.P. "Large-Eddy Simulation on Curvilinear Grids Using Compact Differencing and Filtering Schemes," *Journal of Fluids Engineering*, Vol. 124, No. 4, pp. 836-847, 2002.
- [7] Gaitonde, D.V. and Visbal, M.R. "Further Development of a Navier-Stokes Solution Procedure Based on Higher-Order Formulas," AIAA Paper 99-0557, 1999.
- [8] Visbal, M.R. and Gaitonde, D.V. "Very High-Order Spatially Implicit Schemes for Computational Acoustics on Curvilinear Meshes," *Journal of Computational Acoustics*, Vol. 9, No. 4, pp. 1259-1286, 2001.
- [9] Morgan, P.E. and Visbal, M.R. and Rizzetta, D.P. "A Parallel High-Order Flow Solver for Large-Eddy and Direct Numerical Simulation," AIAA Paper 2002-3123, 2002.
- [10] Launder, B.E. and Sharma, B.I. "Application of the Energy Dissipation Model of Turbulence to the Calculation of Flow Near a Spinning Disc," *Letters in Heat and Mass Transfer*, Vol. 1, No. 2, pp.131-138, 1974.
- [11] Gordnier, R.E. "Computational Study of a Turbulent Delta-Wing Flowfield using Two-Equation Turbulence Models," AIAA Paper 96-2076, 1996.



# CASE 3: FLOW SIMULATION METHODOLOGY FOR SIMULATION OF ACTIVE FLOW CONTROL

Daniel M. Israel<sup>1</sup> and Hermann F. Fasel<sup>1</sup>

<sup>1</sup>*Department of Aerospace and Mechanical Eng., The University of Arizona, Tucson, AZ 85721*

## Introduction

The Flow Simulation Methodology (FSM) is applied to the proposed experimental geometry. In this approach only the largest scales of motion need to be resolved, while in regions where there are no large coherent turbulent structures a state of the art RANS model is recovered. This allows us to obtain good results with fewer than three million grid points for a 3-D calculation.

The simulations performed for this workshop build on our extensive previous work with this geometry, as well as our simulations of the experiments of Seifert and Pack [1, 2, 3, 4]. We have performed both laminar [5] and turbulent [6] simulations for the Seifert and Pack geometry. Lower Reynolds number ( $Re = 10^5$ ) turbulent cases have been computed in both 2-D and 3-D. Additionally, 2-D simulations were performed at  $Re = 10^6$ . The same geometry was also used to test closed loop control strategies [7]. For these earlier investigations a high order (fourth-order in time and space) explicit finite difference code was employed. This code was a curvilinear coordinate extension of previous codes developed for transition research, and consequently was designed to accurately predict the growth rates of disturbances.

For this CFD challenge the computational cost of using an explicit code, especially in 3-D, was unacceptably high. For this reason we have implemented our FSM approach [8, 9] in the CFL3D code developed at NASA Langley. This is a second order implicit thin-layer Navier-Stokes code. All the results submitted for this workshop were performed using this code, with the viscous terms activated in all three coordinate directions.

## Solution Methodology

Details regarding CFL3D can be found in the *CFL3D User's Manual* [10]. Implementation of the FSM (described below) does not require changes to the solution methodology of CFL3D. Since the FSM is a time dependent model, all simulations were run in an unsteady fashion using the second order  $\tau$  – TS pseudo-time iteration scheme.

## Model Description

In order to bridge the gap between RANS and LES Speziale [11] proposed a methodology for computing turbulent flows, which we later called Flow Simulation Methodology. In the FSM, in which a contribution function is introduced which compares the local grid resolution relative to some local turbulent length scale in order to provide the correct magnitude of the turbulent stresses. The contribution function is designed so that in the limit of high resolution the Reynolds stresses vanish, yielding a DNS. For the limit of low resolution, the contribution function goes to unity, yielding a RANS. The subgrid stress is then computed as

$$\tau_{ij} = f_{\Delta} R_{ij}^{\text{RANS}}, \quad (1)$$

where  $f_{\Delta}$  is the contribution function.

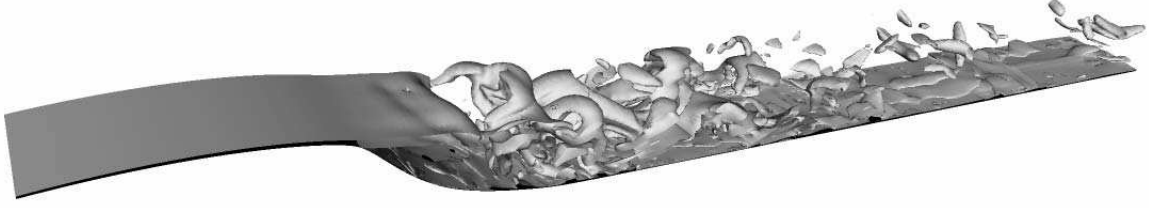


Figure 1: Instantaneous iso-surface of total vorticity.

The FSM differs from typical hybrid or zonal models in two important ways. First, since the contribution function is a time and space varying function, there is no need to specify a priori which regions of the flow are computed as RANS and which as LES or DNS. Second, since a single underlying RANS model is used, the FSM is consistent in its limits; as opposed to zonal models which involve the ad-hoc patching of two unrelated models.

For the simulations presented here, the underlying RANS model is an Explicit Algebraic Stress Model (EASM) [12, 13]. To obtain the required turbulent length scales, the  $k - \varepsilon$  equations are solved. No ramping functions are used in the evaluation of the eddy-viscosity. However, in order to eliminate the near wall singularity in the  $\varepsilon$  equation an  $f_{\varepsilon 2}$  damping function is employed [14]. At present, the FSM implementation in CFL3D is only applied to the linear eddy-viscosity terms so the non-linear terms in the EASM are not used in these simulations.

Several variant forms of the contribution function have been proposed. In the present case the following form is used:

$$f(\Delta, L, L_K) = \frac{C_D \Delta^{2/3} - L_K^{2/3}}{L^{2/3} - L_K^{2/3}},$$

where  $\Delta = (\Delta x \Delta y \Delta z)^{1/3}$ , and the turbulent length scales were estimated using  $L = k^{3/2}/\varepsilon$ ,  $L_K = (\mu^3/\varepsilon)^{1/4}$ .  $C_D$  is a constant which roughly represents the number of grid points per resolved structure. Clipping is applied to insure that  $0 < f_\Delta < 1$ . This function is designed so that the RANS limit is reached as the grid spacing approaches the integral scale, and the DNS limit as the grid spacing approaches the Kolmogorov length scale. The specific form is motivated by a Kolmogorov inertial scale five-thirds decay, however this should not be considered a rigorous justification of this form since we do not expect to see a significant inertial spectrum in the flows we are investigating.

A typical instantaneous flow field is shown in figure 1. One can clearly see the development of large turbulent structures in the recirculation region whereas the oncoming turbulent boundary layer is steady.

## Implementation and Case Specific Details

A nearly orthogonal grid is employed which consists of a two-dimensional body fitted grid over the model which is then extruded in the spanwise dimension. The grid is generated using an elliptic equation [15]. The method is equivalent to the composition of a quasi-conformal mapping and a non-uniform rectilinear stretching. Grid point clustering is achieved by modifying the two independent stretching functions (one in each grid index). The stretching is chosen to cluster points near the wall, and to increase the resolution over



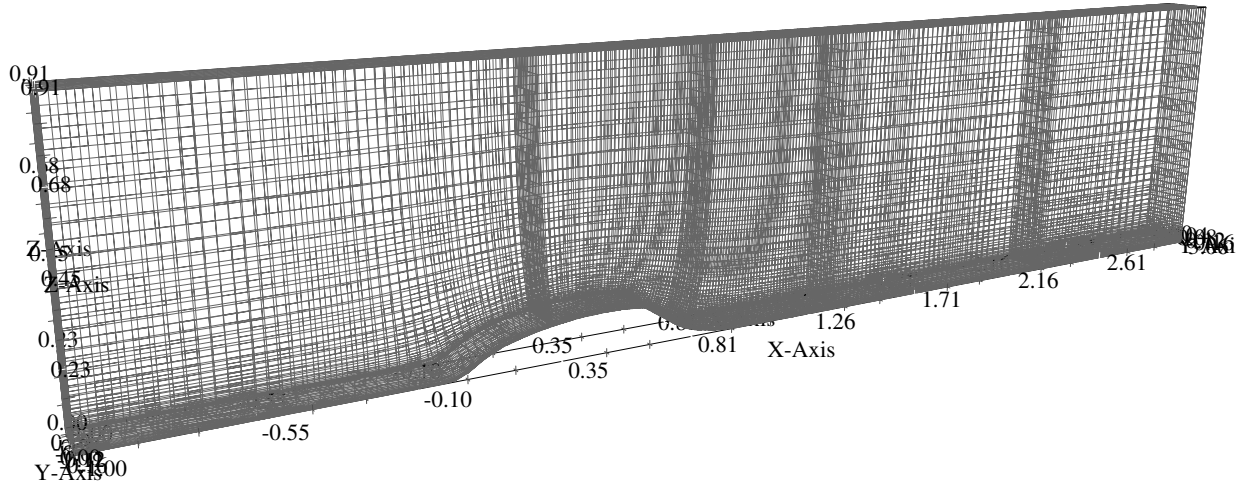


Figure 2: Computational grid. Every 4th point shown in  $x$  and  $y$ .

the concave portion of the ramp. (The quasi-conformal map alone would yield a grid with few points in concave regions.) The grid is shown in figure 2.

The computational domain consists of a portion of the test section extending one chord length upstream of the model, and two chord lengths downstream. The lower surface is a no-slip constant temperature wall. In order to avoid the need for additional grid points, the boundary layer on the upper wall is not simulated. Instead an inviscid surface is used.

At the inflow a turbulent boundary layer is prescribed. For computational efficiency the domain only extends one chord length upstream of the model. (Previous investigations [16] indicate that this is sufficient to avoid undue upstream influence.) Since the only available experimental data for the upstream boundary layer is at  $x/c = -2.14$ , a turbulent boundary layer solver is used to march a solution from the leading edge,  $x/c = -4.61$ , and obtain a boundary layer profile at  $x/c = -1$ . In order to validate this profile, the profile at  $x/c = -2.14$  was also computed; it compares well to the experimental data, see figure 3.

In order to attenuate the outflow disturbances an exponentially stretched rectilinear grid with 100 points in downstream extent is patched on at the outflow and extends to  $x/c = 11$ . The increased grid spacing not only increases the artificial viscosity, but, more importantly, causes the FSM contribution to approach the RANS limit, providing a natural damping region that tends to a steady turbulent boundary layer profile.

Both 2-D and 3-D calculations are performed. As we expected based on earlier work, [6], for the unforced case in which very large amplitude 2-D structures are present, secondary 3-D instabilities become important to the flow, as indicated by the fact that good agreement can be obtained only for 3-D calculations. For the steady suction case the amplitude of the 2-D structures is much reduced, as is the role of the 3-D structures, and good agreement is obtained using 2-D calculations.

Except where otherwise noted, the spanwise domain was  $0.16c$ . Periodicity was enforced on the spanwise end planes. Side wall effects were not accounted for in the primary simulations, although further investigation is underway to examine the influence of the side walls.

The full grid with the ramping region uses  $901 \times 181 \times 17$  grid points in the downstream, wall normal, and spanwise directions, respectively. For reference, this is roughly half the downstream and wall normal resolution and one-tenth the spanwise resolution used in the coarse DNS [17].

The forcing slot was modeled by a transpiration surface with the correct mass flow rate. For unsteady forcing it is important to angle the jet appropriately to assure that the disturbances are introduced into the

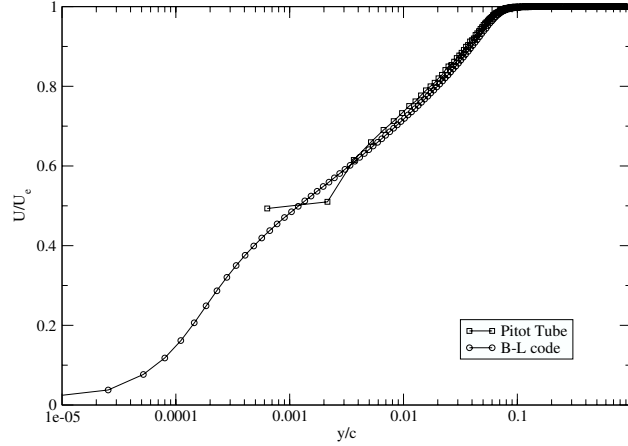


Figure 3: Comparison of the experimental data and turbulent boundary layer solution at  $x/c = -2.14$ .

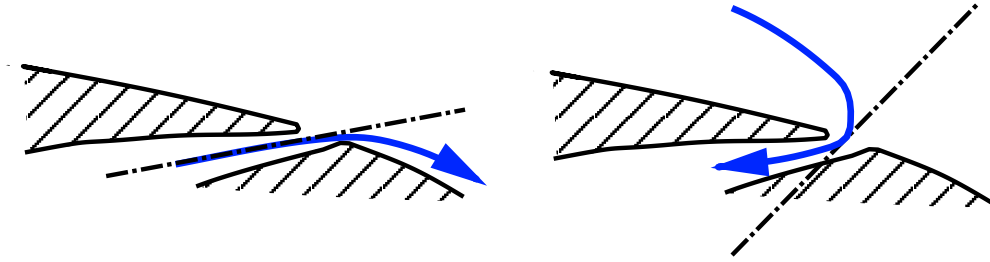


Figure 4: Schematic of slot with blowing (left) and suction (right).

shear layer, rather than blowing through the boundary layer. In the later case we have shown that the effect of the forcing actually decreases for high amplitude forcing [6]. For the suction case, however, wall normal suction was used, since it is not expected that the flow will turn to as steep an angle as the jet nozzle angle (see figure ).

The initial condition for all cases was computed using CFL3D in time steady RANS mode.

## Acknowledgments

We gratefully acknowledge the support of the Air Force Office of Scientific Research (AFOSR) under grant number F49620-02-1-0122, with Dr. Thomas J. Beutner, Program Manager. We would also like to thank Dr. Christopher Rumsey for his help with CFL3D.

## References

- [1] Avi Seifert and LaTunia G. Pack. Active control of separated flows on generic configurations at high Reynolds numbers. AIAA Paper 99-3403, AIAA, June 1999.
- [2] Avi Seifert and LaTunia G. Pack. Sweep and compressibility effects on active separation control at high Reynolds numbers. AIAA Paper 2000-0410, AIAA, January 2000.
- [3] LaTunia G. Pack and Avi Seifert. Dynamics of active separation control at high Reynolds numbers. AIAA Paper 2000-0409, AIAA, January 2000.

- [4] Avi Seifert and LaTunia G. Pack. Separation control at flight Reynolds numbers: Lessons learned and future directions. AIAA Paper 2000-2542, AIAA, June 2000. Fluids 2000.
- [5] Daniel M. Israel and Hermann F. Fasel. Numerical investigation of compressibility effects on active control of boundary layer separation. AIAA Paper 2001-2771, AIAA, June 2001.
- [6] Daniel M. Israel and Hermann F. Fasel. Numerical investigation of turbulent separation control using periodic disturbances. AIAA Paper 2000-0409, AIAA, January 2002.
- [7] Daniel M. Israel and Hermann F. Fasel. A flow simulation methodology for simulation of coherent structures and flow control. AIAA Paper, AIAA, June 2003. Accepted for the 2nd AIAA Flow Control Conference.
- [8] H. F. Fasel, J. Seidel, and S. Wernz. A methodology for simulation of complex turbulent flows. *Journal of Fluids Engineering*, 124:933–942, 2002.
- [9] H. F. Fasel, D. A. von Terzi, and R. D. Sandberg. A methodology for simulating compressible turbulent flows. *FEDSM*, 2003-45334, July 2003. 4th AMSE/JSME Joint Fluids Engineering Conference, Honolulu, Hawaii / Jul 2003.
- [10] Sherrie L. Krist, Robert T. Biedron, and Christopher L. Rumsey. CFL3D user's manual (version 5.0). Technical Report TM-1998-208444, NASA, June 1998.
- [11] Charles G. Speziale. A combined large-eddy simulation and time-dependent RANS capability for high-speed compressible flows. Technical Report AM-97-022, Boston University, September 1997.
- [12] T. B. Gatski and T. Jongen. Nonlinear eddy viscosity and algebraic stress models for solving complex turbulent flows. *Progress in Aerospace Sciences*, 36(8):655–682, 2000.
- [13] Christopher L. Rumsey, Thomas B. Gatski, and Joseph H. Morrison. Turbulence model predictions of strongly curved flow in a u-duct. *AIAA Journal*, 38(8):1394–1402, August 2000.
- [14] Charles G. Speziale and Ridha Abid. Near-wall integration of Reynolds stress turbulence closures with no wall damping. *AIAA Journal*, 33(10):1974–1977, October 1995.
- [15] Ramani Duraiswami and Andrea Prosperetti. Orthogonal mapping in two dimensions. *Journal of Computational Physics*, 98:254–268, February 1992.
- [16] Daniel M. Israel and Hermann F. Fasel. Investigation of separation control in compressible boundary layers using periodic disturbances. AIAA Paper 99-3657, AIAA, July 1999. 30th AIAA Fluid Dynamics Conference.
- [17] D. Postl, S. Wernz, and H. F. Fasel. Direct numerical simulation on the Cray X1. In *CFDVal 2004 Workshop*, 2004. In press.



# CASE 3: CFD VALIDATION OF BASELINE AND CONTROLLED FLOW OVER A SMOOTH HUMP PROFILE

Karthikeyan Duraisamy and James D Baeder

*Department of Aerospace Engineering, Univ. of Maryland, College Park, MD 20742.*

## Introduction

Separated boundary layer flows with subsequent downstream re-attachment are very common in engineering applications. Over the past decade there has been extensive research on control of flow separation using microjet actuators. Accurate numerical solution of such flows continues to be a challenging problem mainly because of their *non-equilibrium* nature. The present work involves the use of Reynolds Averaged Navier Stokes (RANS) and Detached Eddy Simulation (DES) tools in the numerical validation of the ‘Case 3’ problem, which involves high Reynolds number flow over a two dimensional bump. In this paper, the RANS results will be presented and the DES is expected to be completed by the time of the workshop.

## Solution Methodology

For the numerical simulations, the compressible RANS solver OVERFLOW [1] is used. The one equation Spalart-Allmaras (S-A) [2] turbulence model is used for the computations. The inviscid fluxes are computed using a third order upwind scheme with the Roe riemann solver. Alternatively, second or higher order central differencing can also be used. The viscous terms are computed using second order differences. Time accurate computations are performed using the implicit second order backwards difference scheme with Newton sub-iterations. For simulations with turbulence model modifications and detached eddy simulations, the TURNS code [3] will be used. The TURNS code solves the compressible RANS equations with the S-A turbulence model along with third order upwinding for the inviscid terms and second order differencing for the viscous terms. The results from the TURNS code are seen to be identical compared to the OVERFLOW code when both programs are run with the same input conditions.

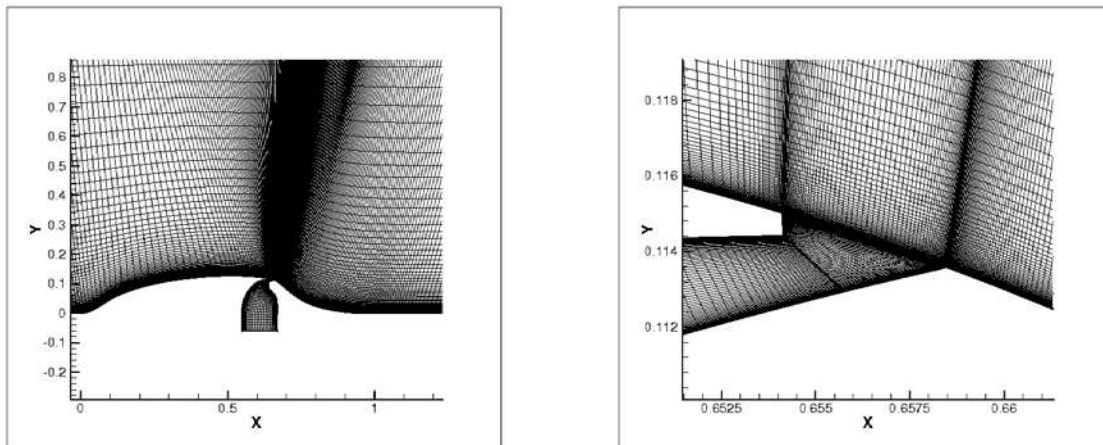


Figure 1: View of Grid 2 (Zoomed up view of slot region on the right).

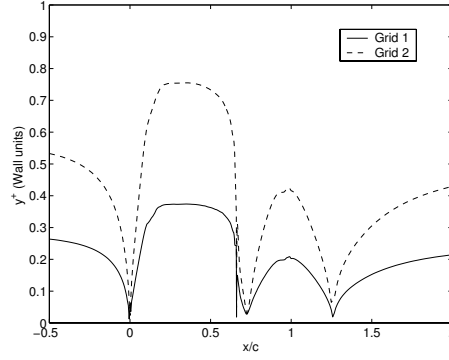


Figure 2: Wall normal spacing.

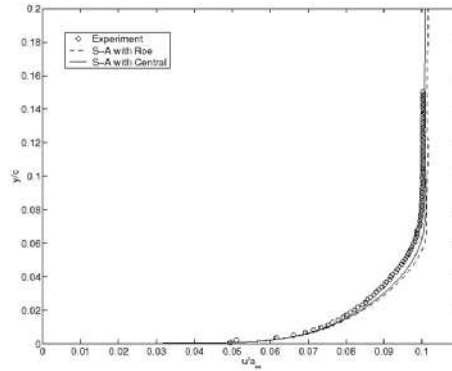


Figure 3: Upstream Velocity ( $x/c=-2.14$ )

The 4-Block structured grids (Fig. 1 shows the coarse grid) provided by the workshop organizers are used in the simulations. The fine grid (Grid 1) has 210060 points and the coarse grid (Grid 2) uses every other point of the fine grid. Fig. 2 shows that the normal spacing at the wall is less than 1 wall unit for both grids. Also, Grid 1 has around 150 normal points in the upstream boundary layer - hence these grids appear to be sufficient for near-wall RANS calculations. Alternate hyperbolic grids with varying grid point distributions in the shear layer were also used, but will not be reported since the solutions are fairly grid independent when the wall normal spacing is less than 2.5 wall units.

The effect of the steady/oscillatory suction/blowing is modeled as a surface boundary condition on the bottom of the bell-shaped chamber (zone 2). The boundary condition procedure is as follows: The density and pressure are extrapolated from the interior of the flow field and the momentum components are specified in accordance with the known mass-flow rate. Alternately, extrapolating the stagnation enthalpy instead of density did not make a significant difference. For the no-flow case, this boundary is treated like an inviscid wall.

The upstream boundary ( $x/c=-6.39$ ) was treated as a subsonic inflow condition with characteristic extrapolation. The resulting inlet profile at  $x/c=-2.14$  is shown in fig. 3. The downstream ( $x/c=4.0$ ) boundary conditions are set by specifying the back pressure and extrapolating all the other primitive variables.

## Implementation and Case Specific Details

The flow in question is a non-equilibrium flow and hence separation and re-attachment could involve unsteady vortex shedding. Reynolds averaging can be expected to cause errors in the final solution because of the difficulty in characterizing the different scales that contribute to mixing. However, before using a higher

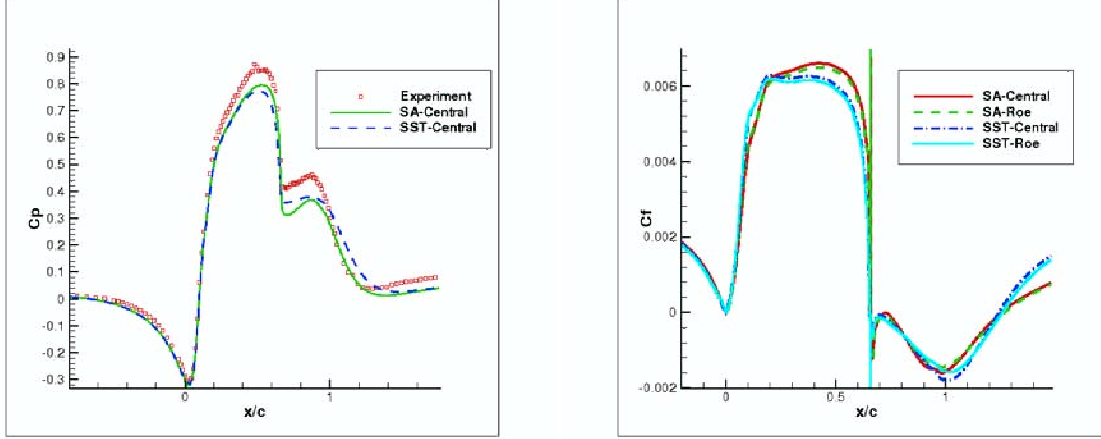


Figure 4: Comparison of Turbulence model and Inviscid differencing with 2D computations using Grid 2

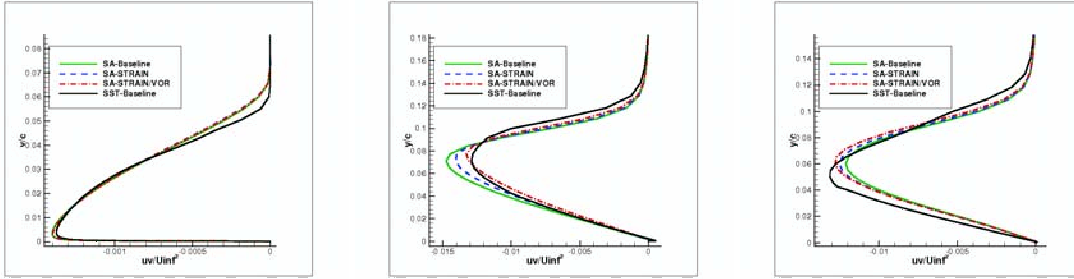


Figure 5: Reynolds stress prediction with the SA models and SST model at  $x/c$  locations: -2.14, 1.0 and 1.2 (from left to right) with Grid 2

end model like hybrid RANS-LES, it is necessary to ensure that the RANS solution is not affected by other procedures within the framework.

The one equation Spalart-Allmaras and two equation Menter SST [4] models are used. Fig. 4 shows the results of a 2D simulation. The difference between upwinding and central differencing is found to be very small. Both turbulence models under-predict the suction peak and the separation region and extent is poorly predicted. *The effect of grid adaptation and refinement in the separated region and around the shear layer did not result in any improved predictions.*

The S-A model [2] uses a production term given by:

$$P = c_{b1} \hat{S} \nu_t, \text{ with } \hat{S} = S + \frac{\hat{\nu}}{\kappa^2 d^2} f_{v2} \quad (1)$$

Three different choices of  $S$  (from the literature) were used:  $S_{baseline} = \omega$ ,  $S_{strain} = D$  and  $S_{strain,vor} = \omega + 2\min(0, D - \omega)$ , where  $\omega$  and  $D$  are the magnitudes of the vorticity and strain tensors respectively. Fig. 5 shows varied predictions of the Reynolds stress for the no-flow case. The baseline version is used in all the computations that follow.

The experiment is made nominally two dimensional by the introduction of end-plates and hence a full 3D simulation should include them. However, solely for comparison purposes, a 3D simulation was performed with a viscous wall on one side and assuming symmetry at the center-span. Grid 2 was extruded in the span-wise direction consisting of 51 stations with a spacing of  $y^+ = 2$  at the viscous wall. The 3D simulations seem to predict the suction peak more accurately.

For the steady suction case, a mass flux  $(\rho v)/(\rho_\infty U_\infty) = 0.01235$  is specified at the bottom of the bell-shaped chamber. For the oscillatory case, a mass flux  $(\rho(t)v(t))/(\rho_\infty U_\infty) = 0.01235 \sin(2\pi ft)$  is

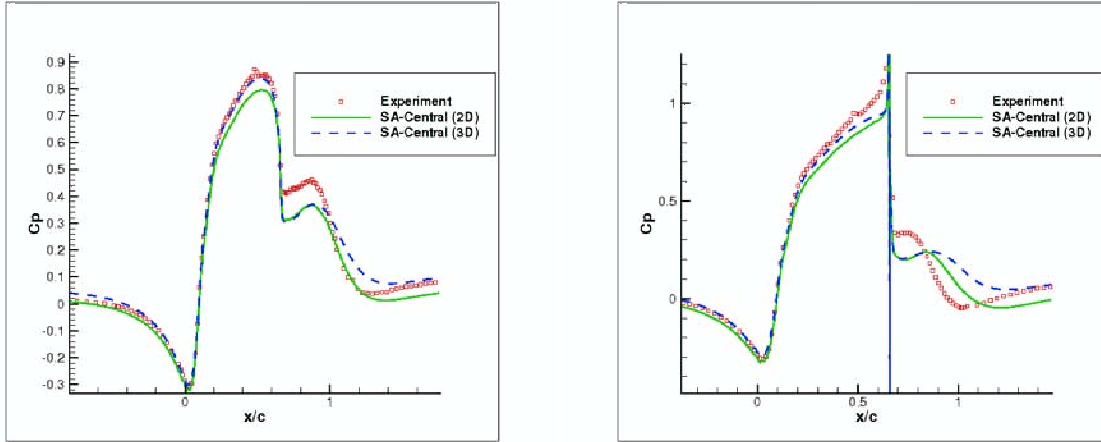


Figure 6: Comparison of 2D and 3D runs for No-flow (left) and Suction (right) cases

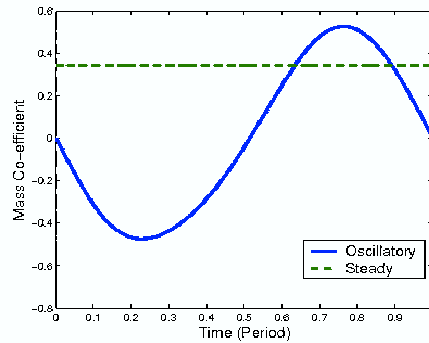


Figure 7: Computed Mass flow ratio across the slot on the hump surface (612 steps per cycle for oscillatory case).

specified. The computed mass flow ratio  $(\hat{m})/(\rho_{\infty} U_{\infty} Area_{slot})$  at the slot is shown in fig. 7. For the the oscillatory case, time accurate computations were performed with 3 different time-steps using 306, 612 and 1224 time-steps per cycle with 5 Newton sub-iterations. The time-average for the latter two cases is seen to be identical. The baseline and controlled pressure and skin friction coefficients (time averaged for oscillatory case) are shown in fig. 8 and corresponding stream-line plots are shown in fig. 9.

Overall, it is seen that discrepancies exist between the RANS results and experiments for both the controlled and uncontrolled cases. These could result from a number of factors:

- Inadequacy of the RANS closure (including the Boussinesq assumption).
- 3D and blockage effects.
- Boundary condition specification (especially for the control cases).
- To an extent, measurement conditions and uncertainties.

## References

- [1] Buning, P., Jespersen, D., Pulliam, T., Chan, W., Slotnick, J., Krist, S., and Renze, K., "OVERFLOW user's manual version 1.8f," NASA Ames Research Center, 1998.
- [2] Spalart, P. and Allmaras, S. "A One Equation Turbulence Model for Aerodynamic Flows," AIAA 92-0439, 1992.



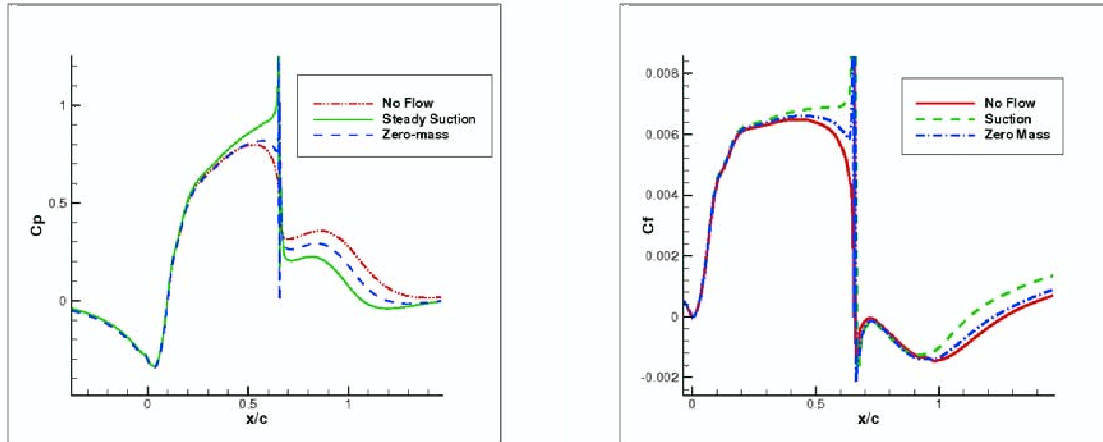


Figure 8: Pressure and skin friction co-efficients using S-A model and Roe Upwinding, Grid 2

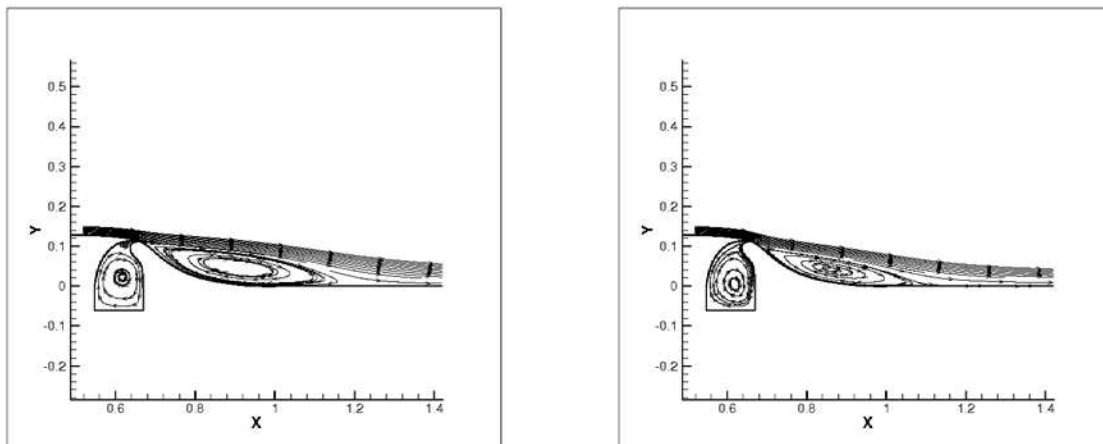


Figure 9: Streamlines for baseline (left) and steady suction cases (right), Grid 2

- [3] Srinivasan, G. and Baeder, J., "TURNS: A Free Wake Euler/ Navier-Stokes Numerical Method for Helicopter Rotors", *AIAA Journal*, Vol. 31, No. 5, 1993.
- [4] Menter, F., "Two Equation Eddy Viscosity Turbulence Models for Engineering Applications," *AIAA Journal*, Vol. 32, No. 8, 1994.

